ACS Catalysis

pubs.acs.org/acscatalysis Research Article

Tunable Surface Cation Arrangements in $Ir_xRu_{1-x}O_2(110)$ and Their Impact on Adsorbate Binding

Suriya Ramasubramanian,[§] Jisu Shin,[§] Tanmayee Kulkarni, Abbul Hasan, David Hibbitts,* and Jason F. Weaver*

Cite This: https://doi.org/10.1021/acscatal.5c09252 Read Online

ACCESS | Metrics & More | Article Recommendations | Supporting Information

ABSTRACT: Advancing methods to control and characterize the local cation arrangements on mixed metal oxide surfaces can afford opportunities for designing catalysts with tunable chemical properties. Here, we show that $Ir_xRu_{1-x}O_2(110)$ solid solutions with variable near-surface cation arrangements can be synthesized by annealing IrO_2/RuO_2 layered structures under mild oxidizing conditions in ultrahigh vacuum. Temperature-programmed desorption (TPD) of adsorbed N_2 and atomic O provides a quantitative probe of the Ir and Ru populations in coordinatively unsaturated (cus) binding sites (M_{cus}) and their nearest-neighbor subsurface sites (M_{subcus}), due to the strong, highly localized influence of these cations on N_2 and O binding. The resulting M_{cus}/M_{subcus} configurations remain stable up to at least 650 K, a temperature range relevant for catalytic studies. Heating IrO_2/RuO_2 layered structures to ~800 K induces rapid Ru−Ir intermixing and drives Ru enrichment in the near-surface region. TPD measurements show that Ru strongly favors incorporation into cus-sites during our heating protocol and begins to occupy subcus-sites only after the Ru_{cus} population approaches saturation. After extended heating, the surface is dominated by Ru_{cus} over Ru_{subcus} motifs (Ru/Ru_2) characteristic of pure $RuO_2(110)$, with small populations of Ru/Ir_2 and Ru/IrRu. Density functional theory (DFT) predicts binding-site distributions for O-terminated surfaces that closely match those determined from TPD. DFT reveals that enhanced O binding on Ru_{cus} relative to Ir_{cus}, along with stabilization by neighboring Ir_{subcus} atoms, drives Ir−Ru interchange to selectively form Ru/Ir_2 motifs and promote Ru occupation of subcus sites after cus sites are filled. Together, these results provide insight into the synthesis and characterization of mixed $Ir_xRu_{1-x}O_2(110)$ surfaces and demonstrate that controlling near-surface cation arrangements offers a promising route to tuning the chemical properties of mixed-oxide catalysts.

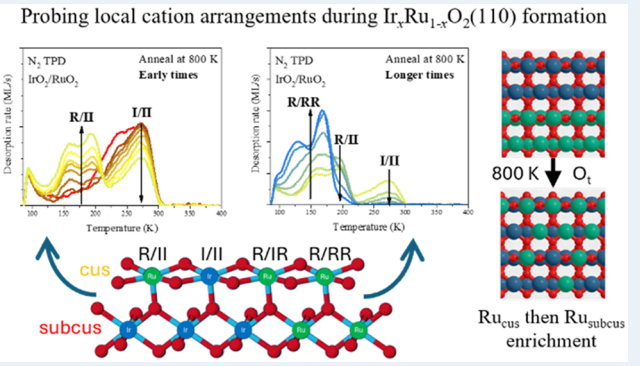

KEYWORDS: *IrO_2, RuO_2, rutile oxide, adsorption, ligand effect, mixed metal oxide, OER*

INTRODUCTION

Mixed Ir−Ru oxide catalysts have been widely investigated for the electrochemical oxygen evolution reaction (OER) and also hold promise for advancing other catalytic transformations. Pure RuO_2 is highly active for the anodic OER but lacks the stability required for practical use due to facile dissolution of Ru under acidic conditions. In contrast, IrO_2 provides superior stability but is less active than RuO_2. Combining IrO_2 and RuO_2 in mixed oxides seeks to integrate the high activity of RuO_2 with the high stability of IrO_2 into a single material.[1−10] Both core−shell structures and solid solutions of IrO_2−RuO_2 have exhibited enhanced OER performance,[4,11,12] but the origins of this improvement remain incompletely understood. In addition, IrO_2 is a highly active catalyst for the complete oxidation of light alkanes, and its combination with RuO_2 can further increase activity,[13−17] affording opportunities to develop efficient alkane oxidation catalysts with reduced Ir content.

Understanding the relations between atomic-scale structure and surface chemical properties is critical for rationally designing mixed metal oxide catalysts, including Ir−Ru oxides. Rutile RuO_2 and IrO_2 are closely lattice-matched, which facilitates the growth of epitaxial IrO_2−RuO_2 heterostructures, and they exhibit high mutual solubility, forming $Ir_xRu_{1-x}O_2$ solid solutions over the entire range of composition.[18−20] Previous studies indicate that the enhanced stability of mixed Ir−Ru oxides relative to RuO_2 arises primarily when IrO_2 is located near the surface, rather than from changes in the bulk electronic structure associated with atomic-scale mixing, as the presence of Ir can protect the underlying Ru from

Received: December 25, 2025
Revised: February 10, 2026
Accepted: February 13, 2026

dissolution.[5,21] Likewise, $Ir_xRu_{1-x}O_2$ solid solutions have been reported to undergo Ir surface enrichment during the OER, leading to improved stability.[11] Notably, stronger binding of chemisorbed oxygen on coordinatively unsaturated (cus) Ir sites has been proposed to drive this Ir surface enrichment under reaction conditions.[11,22]

Recently, we discovered that the local cation environment strongly influences adsorbate binding on single-layer (1L) compared with multiple-layer (*n*L) IrO_2 and RuO_2 films of IrO_2−RuO_2(110) heterostructures.[23] In particular, temperature-programmed desorption (TPD) experiments and density functional theory (DFT) calculations show that adsorbed N_2 and on-top O atoms (O_t) bind more weakly on 1L-IrO_2/RuO_2 compared with *n*L-IrO_2 by ∼11 and 25 kJ/mol, respectively, but more strongly by the same amounts on 1L-RuO_2/IrO_2 than on *n*L-RuO_2. These contrasting behaviors give rise to distinct TPD signatures for N_2 and O_t on the single and multiple-layer oxides. This prior work establishes that O_t binds more strongly on Ru than Ir cus-sites, in contrast to expectations from examining pure metal oxides, as O_t binds stronger to IrO_2 than to RuO_2. N_2 binds more strongly on Ir cus-sites, and the binding of both adsorbates is further strengthened when Ir rather than Ru is located in the subcus sites. For example, a Ru_{cus} site over two Ir_{subcus} sites (Ru/Ir_2) binds O_t atoms more strongly than any other local cus/subcus arrangement, including pure IrO_2(110), suggesting that reaction conditions can induce specific cation configurations not previously recognized.

DFT calculations examined $Ir_xRu_{1-x}O_2$ solid solutions and showed that the binding properties of the single- and multiple-layer oxide films are governed primarily by the identity of the cus binding site and the two subcus cations positioned directly beneath it, with cations in other nearby sites having little impact.[23] Electronic structure analysis explains both of these site and ligand effects, showing that the pronounced role of subcus cations originates from localization of the σ system involved in adsorbate bonding and the resultant charge accumulation on the subsurface O atom beneath the cus site. This charge is more effectively stabilized when Ir rather than Ru occupies the subcus positions.

These highly localized effects may strongly impact the catalytic behavior of mixed Ir−Ru oxides and are critical to understand for the rational design of catalysts with optimal Ir−Ru surface site arrangements, particularly those that minimize Ir content while preserving desirable properties. Significantly, a recent study shows that solid-solution $Ir_xRu_{1-x}O_2$ catalysts with well-dispersed Ir achieve high stability during the OER even at Ir contents as low as 14%.[24] Using DFT-guided Monte Carlo simulations, those authors predicted that at low total Ir concentrations and high O_t coverages, Ir preferentially occupies subcus sites of sufficiently small $Ir_xRu_{1-x}O_2$ nanoparticles, while scarcely populating surface sites, and that the subcus Ir stabilizes neighboring cus Ru atoms beyond what is observed for pure RuO_2(110). This study illustrates how the local surface-subsurface cation arrangements can improve $Ir_xRu_{1-x}O_2$ catalyst performance while minimizing Ir usage. Notably, however, experimental determination of the cation distribution among near-surface sites remains challenging and was not reported.

In the present study, we investigated the formation of $Ir_xRu_{1-x}O_2$ solid solutions by annealing IrO_2/RuO_2 layered structures under mild oxidizing conditions in UHV. From TPD of adsorbed N_2 and O_t, we show that Ru preferentially replaces Ir in cus sites during the early stages of cation intermixing, and starts to populate subcus sites only after nearly saturating the cus sites. DFT calculations for bare and O_t-terminated surfaces predict binding-site distributions for O_t-terminated surfaces that agree closely with those obtained from TPD, indicating that oxygen adsorption trends govern the M_{cus}/M_{subcus} relative populations established during our heating treatments, even as those heating treatments occur at low O_t coverages. Importantly, these results demonstrate that annealing layered IrO_2/RuO_2 structures for varying times provides a route to generate mixed $Ir_xRu_{1-x}O_2$(110) surfaces with tunable surface−subsurface cation arrangements that remain stable at catalytic temperatures, thereby enabling control over adsorbate binding and direct evaluation of its impact on surface reactivity.

COMPUTATIONAL DETAILS

Periodic plane-wave DFT calculations were carried out, as described elsewhere,[23] using the Vienna ab initio simulation package (VASP)[25−28] as implemented in the computational catalysis interface (CCI).[29] The Perdew−Burke−Ernzerhof (PBE)[30] exchange−correlation functional was employed and plane waves were constituted of projector augmented wave pseudopotentials (PAWs) with an energy cutoff of 400 eV.[31,32] Prior work[33] has demonstrated that the electronic structures of these metallic oxides are overlocalized by hybrid functionals leading to unphysical unpaired electrons and magnetic moments, motivating our use of the PBE functional. Calculations of the oxides were run with second-order Methfessel-Paxton smearing with 0.2 eV width.

Figure 1 shows a ball and stick model of the rutile MO_2(110) surface formed by IrO_2 and RuO_2. The MO_2(110) surface has a rectangular unit cell and is composed of alternating rows of coordinatively unsaturated metal atoms (M_{cus}) and bridging O atoms (O_{br}) along the [001] direction. The M_{cus} and O_{br} atoms each have single coordination

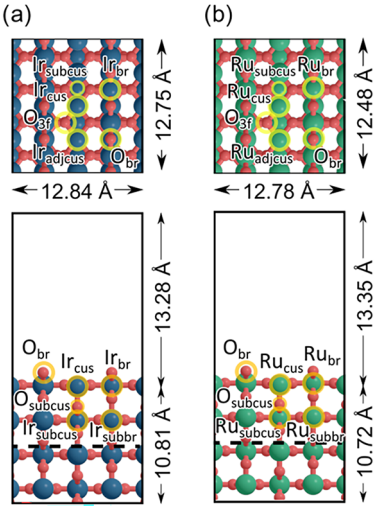

Figure 1. Top and side view of (a) IrO_2(110) and (b) RuO_2(110) with a bridging O atom (O_{br}), cus metal atom (M_{cus}), 6-fold coordinated surface metal atom (M_{br}), subsurface metal atom beneath the cus site (M_{subcus}) that interacts with the cus site through a subsurface O atom (O_{subcus}), and a subsurface metal atom beneath O_{br} and M_{br} atoms (M_{subbr}). Atoms beneath the dashed lines were fixed at their bulk positions during DFT calculations. Green atoms represent Ru, blue atoms represent Ir, and red atoms represent O.

https://doi.org/10.1021/acscatal.5c09252
ACS Catal. XXXX, XXX, XXX−XXX

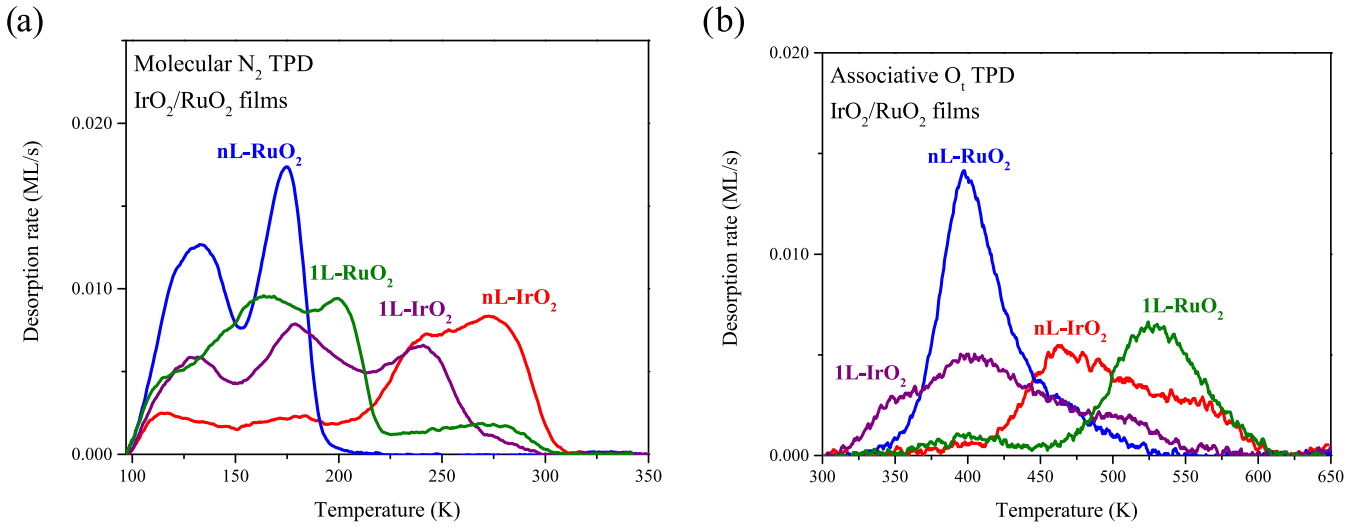

Figure 2. TPD spectra of (a) molecularly adsorbed N_2 and (b) O_2 via O_t recombination for 1L and nL $IrO_2/RuO_2(110)$ and $RuO_2/IrO_2(110)$ surfaces.[23]

vacancies due to a decrease in bond coordination relative to bulk MO_2; the M_{cus} atoms have 5-fold coordination, whereas bulk M atoms have 6-fold coordination, and O_{br} atoms have 2-fold coordination, whereas bulk O atoms have 3-fold coordination. The coordination vacancy on the M_{cus} atom is directed along the surface normal and lies in the axial position of the local octahedral geometry. An O atom (O_{subcus}) occupies the axial position directly beneath the M_{cus} atom, and is bonded to two subsurface cations (M_{subcus}). The identities of these two M_{subcus} cations strongly influence the binding of N_2 and O atoms on the M_{cus} site,[23] an effect exploited in this study to characterize mixed Ir−Ru oxide surfaces. Because the M_{cus} atoms are the active adsorption sites of $IrO_2(110)$ and $RuO_2(110)$, an adsorbate coverage of 1 ML ("monolayer") is defined as the density of M_{cus} atoms on the (110) surfaces. Prior studies show that molecular N_2 adsorbs in an upright configuration on top of the M_{cus} atoms of these oxides,[19,34,35] while O_2 undergoes facile dissociative chemisorption on the M_{cus} rows at 300 K and produces O atoms that adsorb directly on-top (O_t) of M_{cus} atoms (Figure 1).[36−40]

EXPERIMENTAL SECTION

The experiments were performed in an UHV chamber with a base pressure of 3.0×10^{-10} Torr, the details of which have been reported previously.[41−44] Briefly, the chamber is equipped with an inductively coupled RF plasma source (Oxford Scientific Instruments) for generating atomic oxygen beams, two electron-beam metal evaporators (McAllister Technical Services) for the deposition of metallic Ir and Ru, an ion source (SPECS), a low energy electron diffraction (LEED) optics (SPECS), and a shielded quadrupole mass spectrometer (Hiden HAL 511/3F PIC) for temperature-programmed desorption (TPD). The chamber is also equipped with a dual Mg/Al anode X-ray source and a hemispherical analyzer (SPECS) for X-ray photoelectron spectroscopy (XPS).

The circular Ru(0001) single crystal (9 mm × 1 mm) was attached to two 0.38 mm tungsten wires mounted onto an LN_2 cooled sample holder. A type K thermocouple was spot-welded onto the back side of the sample for temperature measurements. Resistive heating, controlled using a PID controller that varies the output of a programmable DC power supply, supports linear ramping from 85 to 1450 K and maintaining a desired temperature. The sample was cleaned by alternating rounds of Ar^+ sputtering (2 keV) at 900 K and annealing in an O_2 background of 5×10^{-7} Torr both at 1000 K, and finally annealing in UHV at 1400 K for several minutes. This procedure produces a high level of surface crystallinity and cleanliness as supported by LEED and XPS.

Growth of Epitaxial Film Structures

$IrO_2(110)$ films were grown stepwise on $RuO_2(110)$ by Ir vapor deposition in UHV, following the previously reported "template-assisted growth" method.[18,45] The $RuO_2(110)$ substrate was prepared as a ∼22-layer film by oxidizing Ru(0001) with an atomic oxygen beam (SI, Section S1). Close lattice matching facilitates epitaxial growth of $IrO_2(110)$ on $RuO_2(110)$ ($\Delta a/a = +0.3\%$, $\Delta c/c = +1.5\%$), and mixing of Ir and Ru was avoided by maintaining the substrate temperature below 700 K during film formation.[46] For the complementary case of RuO_2 on IrO_2, a 5.5-layer IrO_2 film was first grown on the 22-layer RuO_2 substrate, followed by deposition of a 4.5-layer RuO_2 film on top of IrO_2 by Ru vapor deposition in UHV, employing the same template-assisted method.

The quantity of $IrO_2(110)$ generated on $RuO_2(110)$ is specified in terms of "layers", where 1 layer (L) is equivalent to the separation of 0.318 nm between the cation planes of rutile IrO_2 measured along the [110] direction. The $IrO_2(110)$ thickness was estimated from the total Ir fluence to surface, after calibrating the Ir flux from measurements of the attenuation of Ru peaks in XPS (SI, Section S2).[19,46,47] The thickness of RuO_2 grown on $IrO_2(110)$ is defined similarly, and was estimated from the attenuation of Ir peaks in XPS (SI, Section S2). The uncertainties in the IrO_2 and RuO_2 coverages generated by vapor deposition are estimated to be about 3% and 9%, respectively, based on flux calibrations. In general, the number of layers should be regarded as an approximation of the quantity of IrO_2 or RuO_2 rather than describing the morphology of the oxide film. Importantly, however, previous measurements using scanning tunneling microscopy (STM) demonstrate that an $IrO_2(110)$ film grows initially in a nearly layer-by-layer mode on $RuO_2(110)$,[18,45] such that $IrO_2(110)$ domains of single-layer (1L) thickness form in coverages up to at least 0.6 layers, before thickening and transforming to a multilayer (nL) $IrO_2(110)$ film. STM measurements also show that the $RuO_2(110)$ substrate becomes completely covered after generating an approximately 2-layer thick $IrO_2(110)$ film.[21]

Cation Mixing by Annealing Epitaxial Layers

Layered $IrO_2−RuO_2$ structures were heated under oxidizing conditions to induce Ir−Ru cation intermixing and form $Ir_xRu_{1-x}O_2$ solid solutions. We examined two structures initially with IrO_2 over RuO_2 (22L-IrO_2/22L-RuO_2 and 6L-IrO_2/22L-RuO_2), corresponding to bulk Ru contents of ∼50% and ∼80%, respectively, and one initially consisting of RuO_2 over IrO_2 (∼5L-RuO_2/6L-IrO_2/22L-RuO_2). Each sample was heated stepwise until the surface composition approached steady state. In each step, the sample was exposed to an O atom beam

https://doi.org/10.1021/acscatal.5c09252
ACS Catal. XXXX, XXX, XXX−XXX

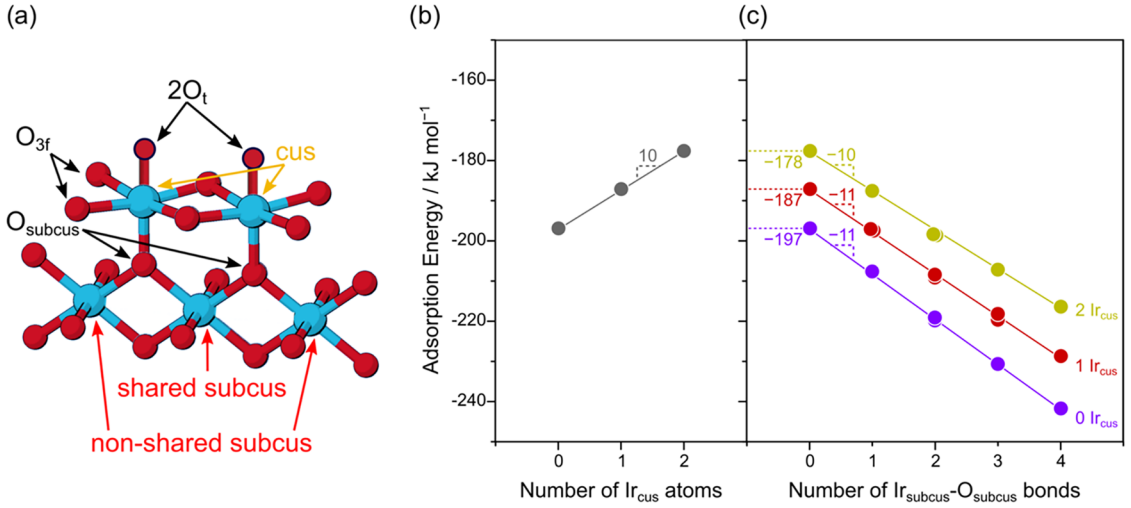

Figure 3. Adsorption energies of O_t pairs on Ru into $IrO_2(110)$ surfaces. (a) Structure of 2 O_t adsorbed showing critical M_{cus} and M_{subcus} atoms. (b, c) $2O_t$ adsorption energies as a function of (b) the number of Ir_{cus} atoms (with 0 Ir_{subcus}−O_{subcus} bonds) and (c) the number of Ir_{subcus}−O_{subcus} bonds. Gold, red, and purple symbols correspond to configurations with 2 Ir_{cus} (0 Ru_{cus}), 1 Ir_{cus} (1 Ru_{cus}), and 0 Ir_{cus} (2 Ru_{cus}) atoms, respectively. Energies for Ir into RuO_2 structures, displaying the same trends, are shown in Figure S6 of the SI, Section S7.

and held at 800 K for 10−30 min, then cooled to 700 K and held for 10 min to ensure complete oxidation. The plasma-generated beam was ∼33% atomic oxygen, with a total O plus O_2 flux of about 0.15 ML s^{-1}. Lastly, the O atom exposure was discontinued at 675 K during cooling to room temperature. This protocol was designed considering the thermal stability of the oxide films and chemisorbed O_t atoms. Previous studies show that IrO_2 and RuO_2 films begin to decompose in UHV near 725 and 825 K, respectively, producing O_2 TPD peaks at 950−1050 K,[48,49] while chemisorbed O_t atoms desorb between ∼300 and 650 K from $IrO_2(110)$ and $RuO_2(110)$.[37−40,50] Thus, the presence of the O atom beam at temperatures of 675−800 K is intended to maintain stoichiometrically terminated $MO_2(110)$ surfaces, and is not expected to result in high coverages of O_t atoms during Ir−Ru mixing. As shown below, these annealing treatments yield surfaces containing coexisting Ir and Ru atoms.

Changes in surface and near-surface composition and local bonding were characterized by XPS and by TPD of adsorbed N_2 and O_t after annealing and cooling. Details of the experiments are given in the SI, Section S3. For each surface, O_2 was dissociatively adsorbed to generate a saturation O_t coverage at 300 K followed by heating to 650 K for the O_t TPD, and the sample was then cooled to 85 K to saturate the surface with molecularly adsorbed N_2, and then heated to 350 K for the N_2 TPD. Importantly, these XPS and TPD measurements follow the progressive evolution of a single specimen rather than independent samples; each heating step continued from the previous one. For example, the sample labeled "95 min" was obtained by subjecting the "80 min" sample to an additional 15 min at 800 K. For the 22L-IrO_2/22L-RuO_2 structure, data were collected at 15 different cumulative heating times, up to a total annealing time of 665 min. The XPS and TPD spectra remained unchanged after repeated TPD cycles (SI, Section S4), confirming that the mixed-oxide surfaces are stable to at least 650 K, the maximum temperature used in TPD. Together, these results demonstrate that stable, mixed Ir−Ru oxide surfaces of varying composition can be reproducibly prepared by adjusting the overall annealing duration of layered IrO_2−RuO_2 films under oxidizing conditions.

Probing Surface and Subsurface Cations with TPD

We recently demonstrated that adsorbate binding energies on IrO_2−RuO_2 surfaces are governed primarily by the identity of the M_{cus} binding site and the two directly underlying M_{subcus} sites, with other nearby cations exerting only minor influence.[23] This behavior was established from TPD experiments and DFT calculations showing that molecular N_2 and associative O_t desorption produce distinct peaks for 1L- versus bulk-like, nL-IrO_2/$RuO_2(110)$ and RuO_2/$IrO_2(110)$ films (Figure 2). Both N_2 and O_t bind more weakly on 1L-IrO_2/RuO_2 than on nL-$IrO_2(110)$, but more strongly by comparable amounts (∼11 and 25 kJ mol^{-1}) on 1L-RuO_2/IrO_2 than on nL-$RuO_2(110)$.[23]

In the present study, we used N_2 and O_2 TPD to monitor how M_{cus} and M_{subcus} populations evolve during Ir−Ru intermixing. Building on our earlier findings, we interpret the TPD data assuming that adsorbate (N_2 and O_t) binding energies depend only on the identities of the M_{cus} binding site and its two underlying M_{subcus} cations. This localized-site framework allows us to approximately determine the occupancy of M_{cus} and M_{subcus} sites as Ir and Ru intermix to form $Ir_xRu_{1-x}O_2$ solid solutions.

RESULTS

DFT Calculations of O_t and N_2 Binding on Mixed Ir−Ru Sites

Our previous work combined the synthesis of epitaxial layered IrO_2/RuO_2 mixed metal oxides with O_2 and N_2 TPD experiments and DFT calculations of O_t and N_2 adsorption on pure, layered and atomically mixed IrO_2 and RuO_2 surfaces. These calculations showed that adsorption energies are primarily determined by three metal cations: the M_{cus} binding site and its two M_{subcus} neighbors, giving rise to six relevant local configurations (Ir/IrIr, Ir/IrRu, Ir/RuRu, Ru/RuRu, Ru/IrRu, Ru/IrIr). Other nearby cations−adjacent cus sites, surface M_{br} atoms, and more distal subsurface cations−have only minor effects.[23]

Ir_{cus} atoms bind N_2 by ∼30 kJ mol^{-1} more strongly than Ru_{cus} but bind O_t ∼11 kJ mol^{-1} more weakly. These opposite trends originate from differences in charge redistribution upon adsorption: O_t depletes 0.2 e at the M_{cus} site (for RuO_2) whereas N_2 accumulates 0.1 e at the M_{cus} site. In contrast, the influence of M_{subcus} sites is similar for both adsorbates: each Ir_{subcus} atom strengthens binding by ∼10 kJ mol^{-1}, and adsorption energies vary linearly with the number of Ir_{subcus} atoms (0−2). These strong ligand effects are localized and directional. M_{subcus} atoms influence adsorption through the O_{subcus} ligand, while O_{3f} ligands around M_{cus} sites play much smaller roles. This arises from the σ-bonding character along the M_{cus}−O_{subcus} bond (in contrast to M_{cus}−O_{3f} bonds) as shown by quasi-atomic orbital analyses.[23]

https://doi.org/10.1021/acscatal.5c09252
ACS Catal. XXXX, XXX, XXX−XXX

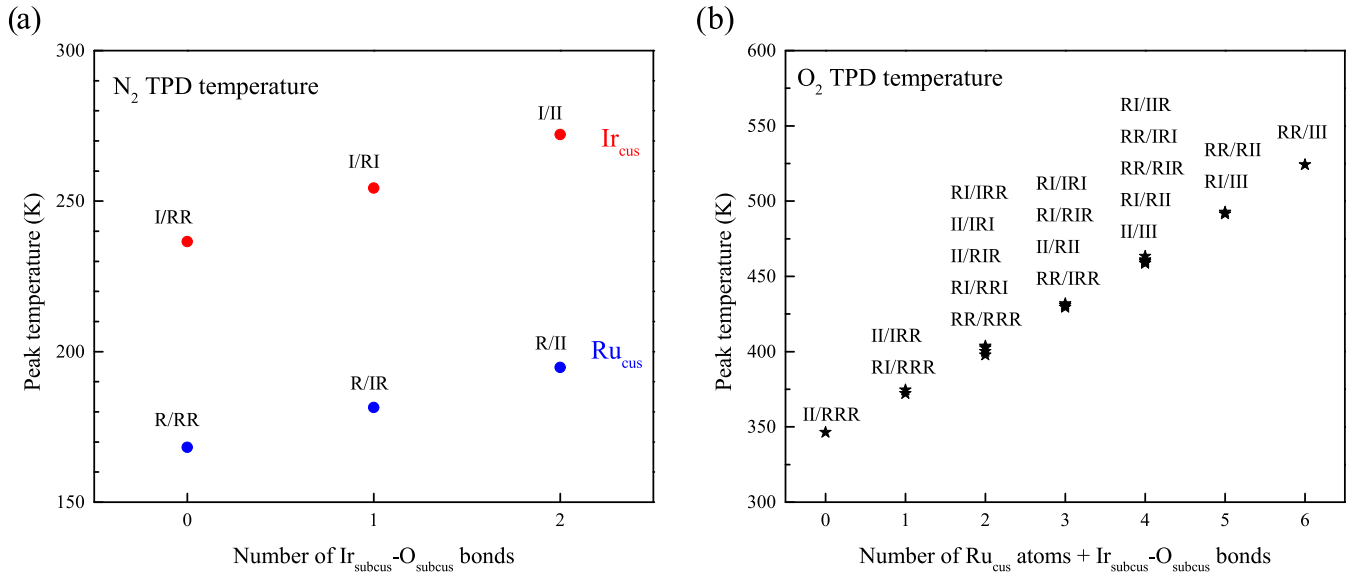

Figure 4. Estimated TPD temperatures for (a) molecular N_2 and (b) associative O_t desorption as a function of M_{cus}/M_{subcus} configuration on $Ir_xRu_{1-x}O_2(110)$ surfaces, respectively. Temperatures are calculated from experimentally determined adsorption energies obtained in prior TPD studies of epitaxial IrO_2/RuO_2 films, with mixed-subcus configurations estimated by linear interpolation and dimer O_t desorption energies obtained by summing monomer contributions (SI, Section S5), as supported by DFT (Figure 3). Monomer and dimer types are listed above the corresponding data points with "R" = Ru and "I" = Ir.

Although our prior DFT work treated atomically mixed surfaces, it did not directly consider the adsorption of O_t pairs on M_{cus} dimers, which may be required for interpreting O_2-formation TPD features if adjacent O_t adsorbates influence one another. For a pair of M_{cus} atoms, three M_{subcus} atoms lie beneath them (Figure 3a), giving 20 possible cation arrangements (SI, Section S5). For a subset of these structures, we show that O_2 dissociation remains facile (SI, Section S6), and that O_t recombination occurs at much lower energies relative to O_2 desorption, consistent with desorption barriers being estimable by the combined binding energies of the O_t pair. As shown in Figure 3b, replacing Ru_{cus} with Ir_{cus} weakens the O_t-pair binding linearly (10 kJ mol^{-1} per Ir_{cus}), in good agreement with the single-O_t behavior mentioned above (11 kJ mol^{-1} per Ir_{cus}); similar behavior is seen in Figure S6 of the SI, Section S7 for Ir exchanges into RuO_2 structures.

Because the two M_{cus} atoms share one M_{subcus} site, we investigated whether this shared site influences a pair of O_t atoms more strongly than either unshared site. Indeed, the Ir_{subcus} in the shared position strengthens binding by ~20 kJ mol^{-1}, twice the ~10 kJ mol^{-1} effect of Ir_{subcus} in unshared positions. When the data are reordered by counting Ir_{subcus}–O_{subcus} bonds (two for the shared site, and one for each unshared site), the adsorption energies collapse onto linear relations with similar slopes but with vertical offsets determined by the identities of the M_{cus} atoms (Figure 3c). Each Ir_{subcus}–O_{subcus} bond strengthens binding by ~10 kJ mol^{-1}, matching our earlier predictions.[23] These results show that O_t–O_t interactions negligibly alter the influence of the M_{cus} identity on O_t binding and that a shared Ir_{subcus} atom can stabilize each of the O_t atoms of a pair without loss of effectiveness. As a result, several of the 20 cation arrangements yield nearly identical adsorption energies (Figure 3c), resulting in 15 distinct behaviors.

Estimated N_2 and O_2 TPD Temperatures from Experimentally Derived Adsorption Energies

The relationships between adsorption energies and the identities of M_{cus} and M_{subcus} sites enable us to estimate TPD temperatures for molecular N_2 and associative O_t desorption from specific M_{cus}/M_{subcus} configurations on $Ir_xRu_{1-x}O_2(110)$ surfaces, using experimentally measured adsorption energies together with interpolation rules supported by DFT. Our prior N_2 and O_t TPD measurements provide adsorption energies for well-defined site ensembles with pure subcus coordination in epitaxially layered structures (Ru/Ru_2, Ru/Ir_2, Ir/Ru_2, Ir/Ir_2), which depend only weakly on other nearby cations. Here, we define a "monomer" as a single M_{cus} site together with its two nearest M_{subcus} atoms, i.e., the local cation motif that primarily determines adsorption on that site. Because the N_2 and O_t adsorption energies on an M_{cus} atom increase approximately linearly with the number of Ir_{subcus} cations,[23] we estimated N_2 and O_t adsorption energies for mixed subcus sites (Ru/IrRu, Ir/IrRu) by linearly interpolating between the experimental values for pure subcus sites. In addition, we calculated associative O_t desorption energies by summing the corresponding monomer adsorption energies determined from TPD. For example, the associative O_t desorption energy for a RuIr/RuIrRu dimer is given by the expression E_{d,O_2}(RuIr/RuIrRu) = E_{d,O_t}(Ru/RuIr) + E_{d,O_t}(Ir/IrRu). Our DFT results (Figure 3) support this representation, indicating that the shared subcus atom influences the O_t-pair adsorption energy approximately twice as strongly as either unshared site. Additional details of these calculations are given in SI, Section S5.

Figure 4 illustrates how the molecular N_2 and associative O_t desorption temperatures vary with the M_{cus}/M_{subcus} configuration. The adsorption energies used in these estimates are derived from prior experimental TPD measurements on epitaxial IrO_2/RuO_2 films that selectively realize the same local M_{cus} sites with pure subcus coordination as those present on atomically mixed $Ir_xRu_{1-x}O_2(110)$ surfaces. In Figure 4a,

https://doi.org/10.1021/acscatal.5c09252
ACS Catal. XXXX, XXX, XXX−XXX

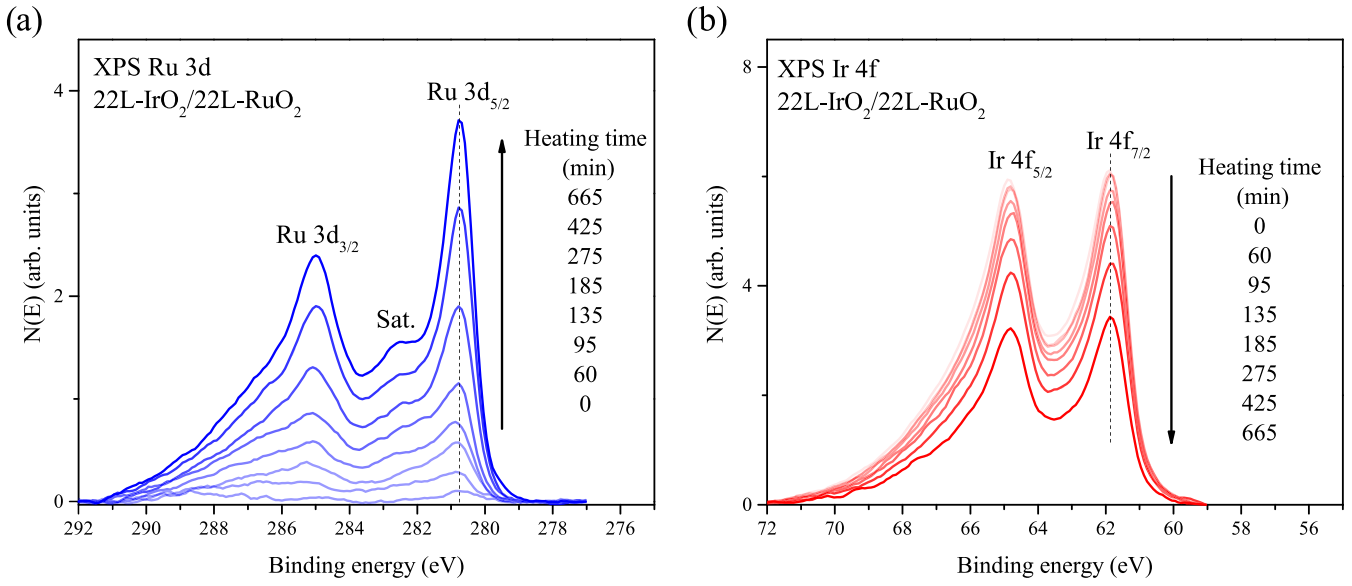

Figure 5. (a) Ru 3d and (b) Ir 4f spectra acquired after heating a 22L-IrO_2/22L-RuO_2 at 800 K under oxidizing conditions for increasing total times (cumulative). The behavior shows that Ru enriches the surface region, while Ir depletes it during heating.

N_2 TPD temperatures are plotted for adsorption on Ru_{cus} and Ir_{cus} sites as a function of the number of Ir_{subcus}−O_{subcus} bonds. Because the M_{cus} identity exerts a stronger influence on adsorption energy than the M_{subcus} environment, the data separate into distinct Ru_{cus}- and Ir_{cus}-derived trends. Within each group, the N_2 TPD temperatures increase approximately linearly with increasing Ir_{subcus}−O_{subcus} coordination, spanning 168−195 K for Ru_{cus} sites and 237−272 K for Ir_{cus} sites.

According to our prior TPD data, the M_{cus} and M_{subcus} identities exert comparable influences on the O_t adsorption energy, with an ∼13 kJ/mol enhancement associated with each Ru_{cus} atom or Ir_{subcus}−O_{subcus} bond.[23] As a result, the O_2 peak temperatures increase nearly linearly with the total number of Ru_{cus} and Ir_{subcus}−O_{subcus} contributions (Figure 4b), with only minor differences among cation arrangements that share the same value of $N(Ru_{cus}) + N(Ir_{subcus}–O_{subcus})$. This behavior produces seven distinct groups of O_2 TPD temperatures at ∼345, 373, 400, 430, 460, 490, and 520 K, corresponding to cation arrangements containing 0 to 6 such contributions. The lowest and highest O_2 desorption temperatures derive from O_t pairs on the Ir_2/Ru_3 and Ru_2/Ir_3 arrangements, respectively. Together, these contrasting N_2 and O_2 behaviors provide a basis for using TPD to monitor the evolution of M_{cus} and M_{subcus} environments as cations intermix during thermal treatment of layered IrO_2/RuO_2 structures.

Heating of 22-Layer IrO_2 on 22-Layer RuO_2

XPS demonstrates that heating IrO_2/RuO_2 layered structures (IrO_2 on top of RuO_2) to 800 K under oxidizing conditions induces Ir−Ru cation mixing while maintaining the +4-oxidation state of both cations. Figure 5 shows Ru 3d and Ir 4f spectra obtained from an initial 22L-IrO_2/22L-RuO_2 layered structure as a function of total heating time at 800 K under an O atom beam. The intervals between heating steps varied, with progressively longer intervals used at extended times. Before heating, the Ru 3d spectrum is nearly undetectable due to attenuation by the overlying 22L-IrO_2 film. This behavior is consistent with the nominal IrO_2 thickness (70 Å), which is about 5 times greater than the inelastic mean free path (IMFP) of the Ru 3d photoelectrons (KE ∼ 970 eV, IMFP ∼ 14 Å)[51] through IrO_2, resulting in a Ru 3d intensity only ∼1% of that for pure RuO_2.

As shown in Figure 5, the Ru 3d intensity increases with heating time while the Ir 4f intensity decreases concurrently. The O 1s peak, associated with O_{br} and lattice O atoms, also shifts to lower binding energy from 530.8 to 530.3 eV as Ru replaces Ir in the near-surface region (SI, Section S8), consistent with the O 1s binding energies characteristic of IrO_2 and RuO_2.[52−54] Similar behavior was observed for the thinner 6L-IrO_2/22L-RuO_2 structure but on shorter time scales (SI, Section S9, Figure S8). As discussed below, intermixing in the 22L-IrO_2/22L-RuO_2 structure slowed beyond a total heating time of 425 min, suggesting that the bulk film composition approached a steady state after the longest treatment (665 min). Collectively, the evolution of the Ru 3d and Ir 4f spectra demonstrates that heating IrO_2/RuO_2 layered structures to 800 K promotes Ir−Ru interdiffusion, leading to progressive replacement of Ir by Ru in the surface region as cations redistribute throughout the oxide film.

XPS further shows that our heating protocol preserves both the Ru^{4+} and Ir^{4+} oxidation states, indicating that the total O and O_2 flux (∼0.15 ML s^{-1}) provides a sufficiently high oxidation rate to stabilize the oxide films at a temperature (800 K) where they would otherwise thermally reduce in UHV, although this flux is not expected to result in appreciable coverages of O_t atoms at these treatment temperatures (800 K). The main Ru $3d_{5/2}$ and Ir $4f_{7/2}$ peaks remain at binding energies of 280.7 and 61.8 eV, as their intensities evolve during heating, and show negligible broadening toward lower binding energies. These characteristics along with the observation that the (110) LEED pattern is maintained on mixing (SI, Section S10) verify that the oxides retain the MO_2 stoichiometry during heating and that metallic Ir and Ru formation is minimal.[52−54] The Ir 4f spectra also maintain a consistent shape throughout heating, whereas the Ru 3d peaks initially exhibit broadening on their high binding-energy sides that diminishes with increasing heating time, along with accentuation of a satellite feature at ∼282.5 eV. These high binding-energy features have been attributed to Ru $3d_{5/2}$ photoelectrons that undergo energy loss via plasmon excitations.[21,55]

https://doi.org/10.1021/acscatal.5c09252
ACS Catal. XXXX, XXX, XXX−XXX

Because such loss processes depend sensitively on the electronic structure near the Fermi level, we attribute the observed changes in Ru 3d broadening to modifications of the valence and conduction band structures accompanying Ir−Ru cation intermixing. Further investigation of these effects is beyond the scope of the present study. Together, the XPS and LEED data confirm that the heating protocol maintains full oxidation of both cations, enabling the preparation of mixed Ir−Ru oxides with variable near-surface compositions while preserving the rutile MO_2 framework.

Near-Surface Composition from XPS

Quantitative analysis of the Ru 3d and Ir 4f spectra shows that the near-surface Ru concentration exceeds the overall bulk composition of the 22L-IrO_2/22L-RuO_2 structure as the cation dispersion approaches steady state after prolonged heat treatments at 800 K. Figure 6 shows Ru and Ir mole fractions as a function of the total heating time, determined from the Ru 3d and Ir 4f areas after correction for atomic sensitivity factors (SI, Section S11). These mole fractions represent the average composition within the XPS sampling depth, with surface layers contributing most strongly to the signal. At the photon energy used ($h\nu$ = 1253.6 eV), we estimate that the surface layer contributes ~18% of the Ru 3d and Ir 4f signals, while the outermost five layers account for approximately 60% of the total intensities (SI, Section S2). The Ru mole fraction increases steadily during early heating but the rate of change decreases markedly above ~275 min, suggesting that the system begins to approach a steady-state composition. After the longest treatment (665 min), the near-surface Ru fraction reaches 58%, exceeding the bulk value of 50% and indicating Ru enrichment in the near-surface region as Ir−Ru intermixing progresses. As shown below, TPD of adsorbed N_2 and O_t corroborates that Ru preferentially occupies the outermost surface layers, consistent with the XPS-derived composition.

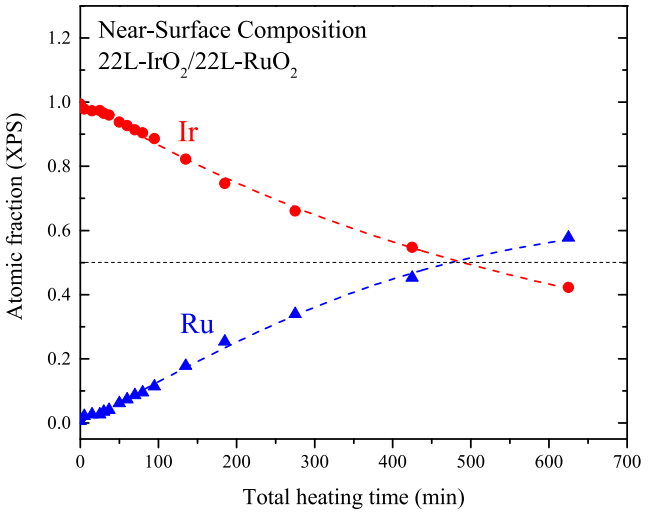

Figure 6. XPS-derived evolution of Ir and Ru atomic fractions in the near-surface region of the 22L-IrO_2/22L-RuO_2 structure as a function of the cumulative heating time at 800 K.

Probing the Outermost Surface Layers: Molecular N_2 TPD

TPD of adsorbed N_2 was used to characterize the evolution of M_{cus} and M_{subcus} sites during thermal Ir−Ru cation intermixing. In each experiment, N_2 was adsorbed to saturation at 85 K, yielding initial coverages near 0.8 ML.[19,23] Before heating, the N_2 TPD spectrum (Figure 7) is characteristic of nL-IrO_2(110), displaying a shoulder at 242 K and a dominant peak at 272 K that correspond to desorption from high and low N_2 coverage configurations along the Ir_{cus} rows, respectively. At high coverage, lateral repulsion destabilizes N_2 adsorbed on IrO_2(110), while desorption from these configurations lowers the coverage and enables N_2 to subsequently desorb from more stable, less crowded arrangements.[19] The weaker features below ~200 K have been attributed to N_2 desorption from kinetically trapped, metastable states formed during low-temperature (85 K) adsorption;[19,23] these states likely originate from physisorbed N_2 in positions available along or between the Ir_{cus} or O_{br} rows.

Changes in the N_2 TPD spectra observed after heating the 22L-IrO_2/22L-RuO_2 structure for up to 135 min are attributed to the selective replacement of Ir by Ru atoms in cus-sites while Ir atoms persist in subcus-sites. Initial heating (up to 37

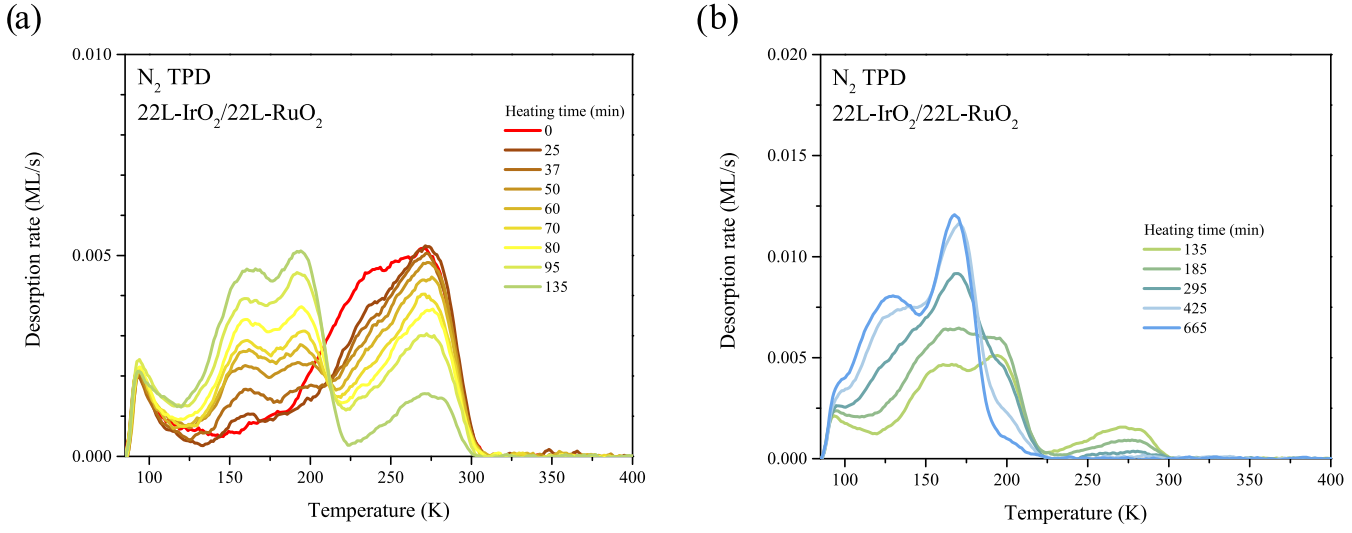

Figure 7. N_2 TPD spectra acquired from the 22L-IrO_2/22L-RuO_2 structure as a function of total heating time at 800 K. N_2 was adsorbed to saturation at 85 K for each experiment. Data are shown for (a) short and (b) long times.

https://doi.org/10.1021/acscatal.5c09252
ACS Catal. XXXX, XXX, XXX−XXX

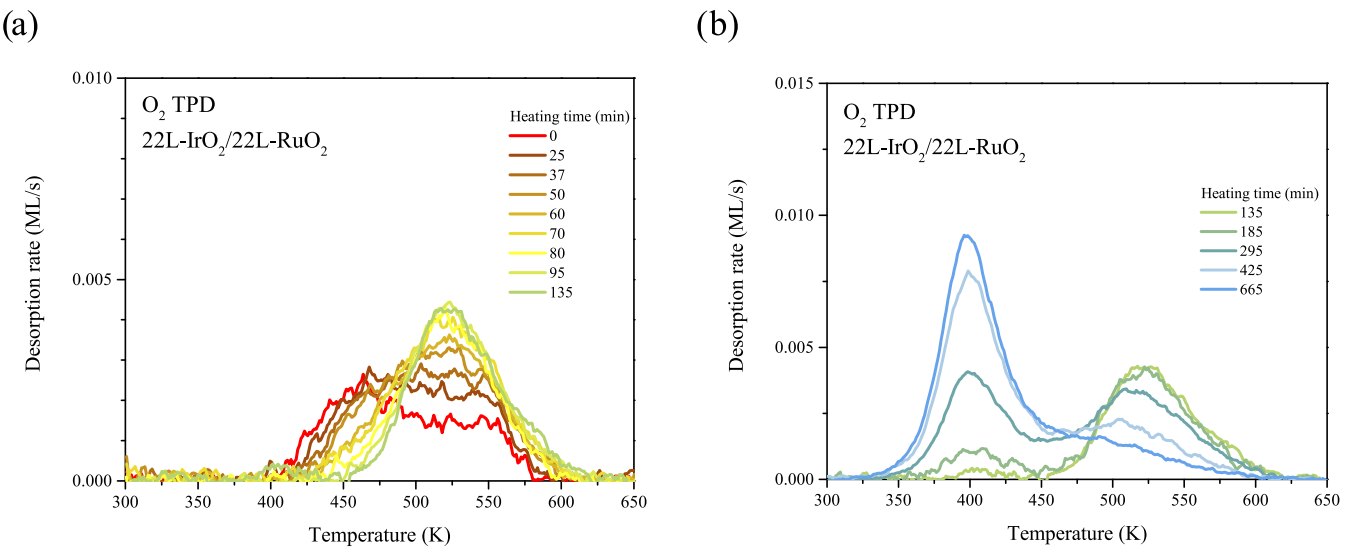

Figure 8. O_2 TPD spectra for O_t associative desorption acquired from the 22L-IrO_2/22L-RuO_2 structure as a function of total heating time at 800 K. In each experiment, a saturation coverage of O_t atoms was generated via the dissociative adsorption of O_2 at 300 K. Data are shown for (a) short and (b) long times.

min) caused the N_2 peak at ∼242 K to diminish markedly without appreciable change in the 272 K peak intensity, while a peak at 160 K emerged and intensified and another at 195 K developed more gradually (Figure 7a). Upon further heating for a total of 135 min, the N_2 TPD intensity above ∼220 K decreased steadily as the 160 and 195 K peaks grew, with the latter becoming more intense. The peaks at 160 and 195 K are consistent with N_2 desorption from high and low coverages on Ru/Ir_2 sites.[23] As discussed above, N_2 desorption from Ir/RuIr and Ir/Ru_2 monomers is expected to produce TPD peaks at ∼237 and 254 K (Figure 4 and Section S5). Because the N_2 TPD intensity above ∼220 K decreases continually during heating—particularly near 240 K at early times—the data strongly suggests that Ru initially populates only cus-sites, avoiding arrangements with Ir_{cus} over Ru_{subcus} cations. Changes in the O_2 TPD spectra as well as DFT calculations further support this interpretation.

The N_2 TPD data also provides evidence that Ru atoms atomically disperse among M_{cus} sites. Specifically, the decrease in the N_2 peak at 242 K accompanied by emergence of the 160 K peak observed during early heating (up to 37 min) is attributed to the formation of isolated Ru_{cus} atoms that disrupt long chains of Ir_{cus} atoms. Because N_2 binds more weakly on Ru_{cus} than Ir_{cus}, desorption from isolated Ru_{cus} sites would occur primarily from crowded configurations, giving rise to a TPD peak at lower temperature than that for N_2 desorption at low coverages on Ru/Ir_2 sites (Figure 4), consistent with the more intense peak at 160 K than 200 K. Desorption from isolated Ru_{cus} sites would also relieve repulsive interactions among the remaining N_2 on Ir/Ir_2 sites by allowing slight lateral expansion along the Ir_{cus} rows,[19] consistent with the more pronounced decrease of the 242 K peak relative to the 272 K peak at early times.

An apparent isosbestic point also develops near 220 K as the annealing time is increased from 37 to 135 min (Figure 7a). This behavior is attributed to a gradual reduction in the influence of coadsorbate repulsions on N_2 desorption from Ir_{cus} atoms as Ru increasingly populates cus sites, leading to the formation of isolated Ir_{cus} configurations. Notably, in our previous work, the high- and low-coverage N_2 TPD peaks from nL-IrO_2(110) (Ir/Ir_2 sites) and 1L-RuO_2 (Ru/Ir_2 sites) decreased and increased proportionally as the 1L-RuO_2 coverage on IrO_2 was raised.[23] The contrasting behavior observed here further supports the conclusion that Ru atoms are well-mixed within the M_{cus} rows and initially form isolated Ru/Ir_2 sites. As the Ru_{cus} concentration increases further, isolated Ir/Ir_2 sites appear to form, as suggested by the diminishing influence of coadsorbate interactions on N_2 desorption from Ir_{cus} sites.

The N_2 TPD spectra indicate that Ru atoms begin to populate subcus-sites at longer heating-times (>∼ 185 min), after most cus-sites have been occupied by Ru. Following 185 min of heating, the TPD intensity above 225 K decreases further while the ∼160 and 200 K peaks grow in intensity and the 160 K feature broadens (Figure 7b). N_2 desorption from high and low coverages on Ru/RuIr and Ru/Ru_2 sites is expected to produce TPD peaks near ∼150 and 181 K vs 130 and 168 K, respectively (Figure 4).[23] The broadening of the ∼160 K peak after 185 min heating is therefore consistent with the initial substitution of Ir by Ru in subcus-sites, and formation of Ru/RuIr monomers. Upon further heating (>∼275 min), the 200 K feature diminishes while a peak at 168 K becomes dominant and another near 130 K emerges. The N_2 TPD spectrum obtained after the longest heating time (665 min) closely resembles that from pure RuO_2(110),[23] though the intensity near 200 K remains somewhat enhanced. This is consistent with a surface dominated by Ru/Ru_2 sites along with smaller amounts of Ru/RuIr and Ru/Ir_2 sites. Overall, the evolution of the N_2 TPD spectra demonstrates that Ru preferentially replaces Ir in cus-sites during the early stages of Ir−Ru cation intermixing, followed by substitution of Ir by Ru in subcus-sites once cus-sites are nearly saturated with Ru. The data further indicate that Ir_{cus}-over-Ru_{subcus} configurations (i.e., Ir/IrRu and Ir/Ru_2) are disfavored during these thermal treatments.

Probing the Outermost Surface Layers: Associative O_t TPD

The evolution of the O_2 TPD spectra from O_t associative desorption (Figure 8) corroborates the trends observed in the N_2 TPD experiments. The O_2 TPD feature for pure IrO_2 (Ir_2−

https://doi.org/10.1021/acscatal.5c09252
ACS Catal. XXXX, XXX, XXX−XXX

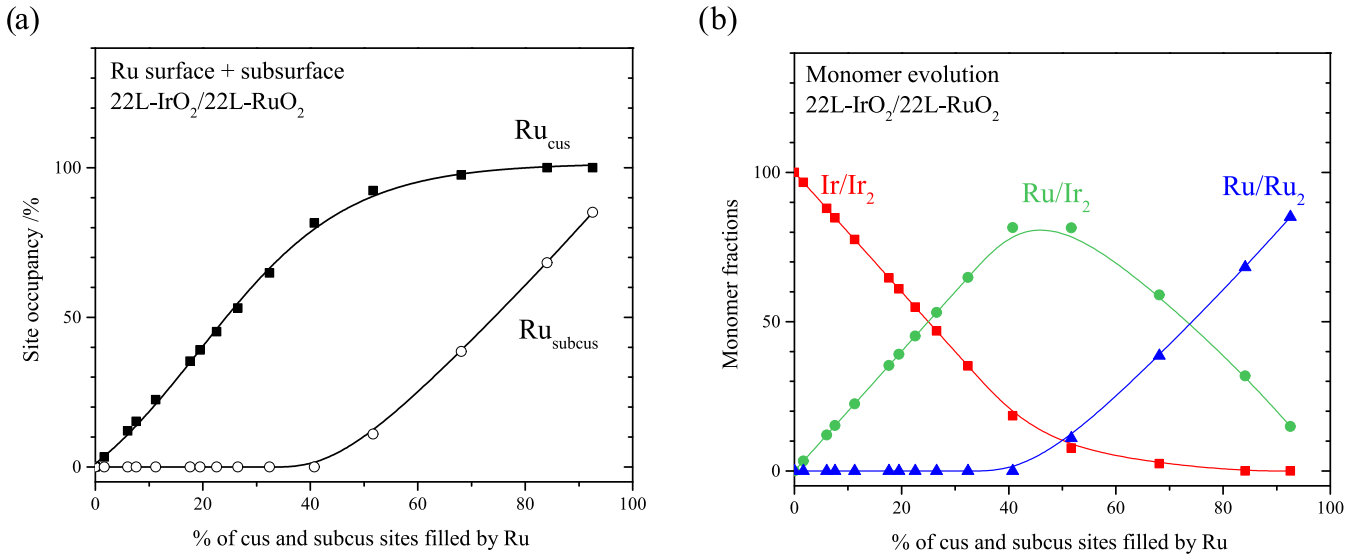

Figure 9. (a) Ru_{cus} and Ru_{subcus} atomic fractions and (b) surface monomer fractions for the 22L-IrO_2/22L-RuO_2 structure as a function of the % of cus and subcus sites filled by Ru. These mole fractions were estimated from fits of the N_2 TPD spectra as described in SI, Section S12. For results from a 6-layer film, refer to SI, Section S14.

Ir_3 dimer sites) exhibits a maximum at about 462 K with a broad tail extending to ~600 K. With limited annealing (<~135 min), the intensity near 462 K decreases, the leading-edge shifts to higher temperature, and the O_2 TPD intensity above ~475 K increases (Figure 8a). The initial decrease in the 462 K feature parallels the N_2 TPD observations, where the desorption feature from Ir−Ir_2 sites diminishes as Ru replaces Ir in cus-sites. At no point during annealing do we see any distinct O_2 TPD features below 400 K.

Among the 20 possible dimer configurations ($2M_{cus}$/$3M_{subcus}$), 12 are predicted to produce O_2 TPD peaks below 460 K (near 345, 373, 400, and 430 K; Figure 4b and Section S5). The absence of such peaks indicates that none of these 12 pair configurations form during the early stages of Ir−Ru intermixing. Ten of these 12 structures contain Ir_{cus}-over-Ru_{subcus} arrangements, while the remaining 2 correspond to high Ru content: Ru_2/Ru_3 and Ru_2/Ru_2Ir. Moreover, of the 10 total configurations that include two or more Ru_{subcus} cations (Section S5), nine are predicted to bind O_t more weakly than the Ir_2/Ir_3 arrangement and would produce O_2 TPD peaks below 460 K (Figure 4b), in contrast to the observed behavior. Thus, in agreement with the N_2 TPD results, the O_2 TPD data indicate that Ir_{cus}-over-Ru_{subcus} configurations are thermodynamically or kinetically disfavored during the early mixing stages, and that Ru preferentially occupies cus-sites before populating subcus-sites.

The decrease in the 462 K feature is accompanied by enhanced O_2 TPD intensity between ~470 and 600 K. For heating times up to ~70 min, this region exhibits a broad, irregular shape that sharpens as a peak near 520 K emerges between 70 and 135 min. As summarized in Figure 4b, 8 out of 20 dimer configurations are predicted to produce O_2 desorption above ~460 K; five with peaks near 460−465 K (Ir_2/Ir_3, RuIr/$RuIr_2$, Ru_2/IrRuIr, Ru_2/RuIrRu, RuIr/Ir_2Ru), and three with peaks above 460 K (RuIr/Ir_3 and Ru_2/$RuIr_2$ near 490 K; Ru_2/Ir_3 near 520 K). Because the O_2 TPD intensity increases predominantly above ~475 K, we conclude that RuIr/Ir_3 sites form preferentially at early heating times, followed by their conversion to Ru_2/Ir_3 sites as heating progresses and the 520 K peak intensifies. This interpretation aligns closely with the N_2 TPD results, which indicate that Ru first occupies cus-sites and later populates subcus-sites as Ir−Ru intermixing advances.

At longer heating times (>~185 min), an O_2 peak emerges at ~400 K, while the 520 K peak gradually diminishes and a broad region between ~440 and 490 K intensifies. The trailing edge of the 400 K peak remains elevated but decreases with further heating, and the overall spectrum progressively approaches that of *n*L-RuO_2. These changes are attributed to the substitution of Ru for Ir at subcus-sites after Ru has largely occupied the cus-sites. Notably, the O_t binding strength on Ru_{cus} sites is expected to weaken as Ru replaces Ir in the underlying subcus-positions. As Ru increasingly occupies the subcus-sites, a series of Ru_{cus}-dimers is predicted to form, each characterized by successively lower O_2 desorption temperatures. Specifically, dimers containing one Ru_{subcus} atom (Ru_2/$RuIr_2$) are expected to desorb O_2 near 490 K, while those with two Ru_{subcus} atoms (Ru_2/RuIrRu and Ru_2/$IrRu_2$) desorb O_2 near 460 and 430 K (Figure 4b). Once Ru fully replaces Ir in the subcus positions, the Ru_2/Ru_3 configuration dominates, producing a peak near 400 K. The overall evolution of the O_2 TPD spectra is thus consistent with the near-complete substitution of Ir by Ru in the subcus-sites after extended heating, as indicated by the continuous decrease in intensity above ~475 K and the concurrent growth of the characteristic 400 K feature. After the longest heating time (665 min), the O_2 TPD spectrum closely resembles that of pure *n*L-RuO_2(110), though the residual intensity above ~475 K indicates a small remaining population of Ru_{cus}-over-Ir_{subcus} arrangements.

Quantifying the Cation Composition in Cus- and Subcus-Sites

Surface fractions of Ir and Ru monomers were estimated as a function of annealing time by fitting the N_2 TPD data; details of the fitting procedure and results are provided in SI, Sections S12 and S13 for 22L- and 6L-IrO_2 films, respectively. Similar fits were not applied to the O_2 TPD data due to the large number of dimer configurations and the resulting complexity of the TPD line shapes. Briefly, the fits included N_2 TPD

https://doi.org/10.1021/acscatal.5c09252
ACS Catal. XXXX, XXX, XXX−XXX

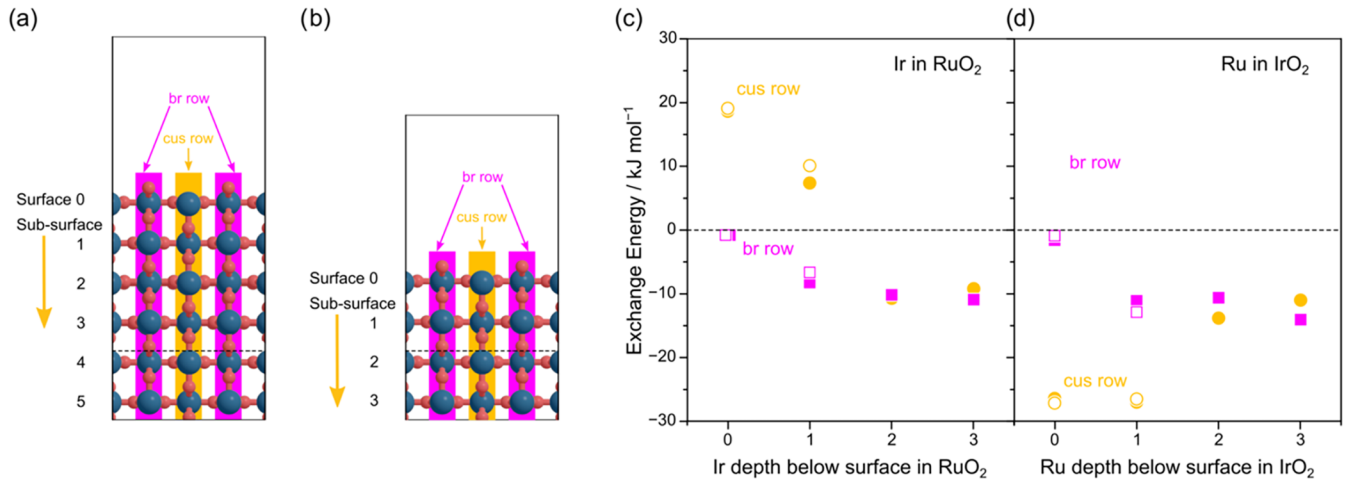

Figure 10. Differential exchange energies of Ir and Ru dopants in RuO_2(110) and IrO_2(110) hosts. (a, b) Side view of the 6-layer and 4-layer (110) surfaces showing labeled *cus* (orange) and *br* (magenta) rows. Atoms beneath the dashed lines were fixed in their bulk positions. (c) Exchange energies of Ir in RuO_2(110) and (d) Ru in IrO_2(110) for the 6-layer (solid) and 4-layer (hollow) models as a function of depth below the surface.

components corresponding to Ir/Ir_2, Ru/Ru_2, and Ru/Ir_2 monomers, with peak positions for the pure cation arrangements determined from reference IrO_2(110) and RuO_2(110) surfaces. At longer annealing times (>∼185 min), the N_2 TPD spectra indicate a transition from Ru/Ir_2- to Ru/Ru_2-like behavior, during which Ru/RuIr sites likely form, as suggested by the broadening of the ∼160 K N_2 peak (Figure 7b). Compared with the Ru/Ir_2 fitting component, the Ru/Ru_2 component is expected to be more reliable because it was derived from measurements on pure RuO_2(110), which contains only Ru/Ru_2 sites. As a result, the Ru/Ir_2 component likely incorporates contributions from Ru/RuIr sites, leading to an overestimation of the Ru/Ir_2 fraction and an underestimation of the Ru_{subcus} fraction at longer annealing times, when Ru begins to occupy subcus-sites. Despite this uncertainty, the fitted monomer and Ru site fractions clearly demonstrate Ru's strong preference for replacing Ir in cus-sites first and subsequently populating subcus-sites during the thermal treatments, resulting in surface compositions that increasingly resemble those of pure RuO_2(110).

Quantitative analysis supports the conclusion that Ru nearly completely replaces Ir in cus-sites before occupying subcus-sites during the heating treatments. As shown in Figure 9a, the Ru_{subcus} population remains negligible while the Ru cus-site occupancy increases to about 82%. Only as the Ru_{cus} fraction nears saturation does the Ru_{subcus} population begin to rise. The final Ru_{cus} and Ru_{subcus} fractions are ∼100% and ∼85%, respectively, with the latter slightly underestimated, as discussed above. As elaborated below, DFT calculations predict that Ru is energetically favored at both cus and subcus sites, and further indicate that the strong preference for first occupying cus sites arises from oxygen-driven Ru−Ir exchange, which stabilizes Ru at cus positions through the formation of strongly bound O on Ru/Ir_2 motifs.

The preferential occupation of Ru in cus sites is also reflected in the evolution of monomer types with increasing Ru content in cus and subcus sites. Our analysis predicts that only Ir/Ir_2 and Ru/Ir_2 monomers coexist for up to ∼40% Ru in cus and subcus sites (Figure 9b). The Ru/Ir_2 fraction increases to 82% (Ir/Ir_2 = 18%) as Ru progressively replaces Ir in cus-sites. Once Ru_{cus} approaches saturation, Ru begins to substitute Ir in subcus-sites, leading to an increase in the Ru/Ru_2 fraction accompanied by a decline in Ru/Ir_2. The Ir/Ir_2 fraction continues to decrease and becomes negligible above ∼68% Ru occupancy of cus and subcus sites. Notably, Ir/Ir_2 and Ru/Ru_2 monomers coexist only over a narrow range of intermediate Ru contents, when both are present at low concentrations (e.g., ∼8% and 11% at 52% Ru; Figure 9b). At the highest Ru concentration (∼93% in cus and subcus sites), only Ru/Ru_2 and Ru/Ir_2 monomers remain, with estimated fractions of 85% and 15%, respectively. The true Ru/Ir_2 fraction is likely smaller than 15% because this value probably includes contributions from Ru/RuIr sites. Overall, these results further show that Ru preferentially populates cus-sites before entering subcus-sites during the heating treatments, ultimately producing a near RuO_2(110) surface. They further demonstrate that distinct monomer populations can be generated through controlled annealing of IrO_2−RuO_2 layered structures, although the range of coexisting states is limited by Ru's strong tendency for cus-sites under the conditions studied.

Interestingly, the TPD data shows that Ru substantially enriches the cus- and subcus-sites even when XPS indicates a relatively low overall Ru fraction. For example, after 135 min of Ir−Ru mixing, the N_2 TPD analysis predicts that the Ru_{cus} fraction is 82% (with Ru_{subcus} ∼ 0; Section S14, Figure S15b), whereas XPS shows a Ru fraction of only 18%. After the longest heating time, Ru occupies ∼93% of the cus and subcus sites, approaching a pure RuO_2 surface, yet the corresponding XPS Ru fraction is only 58%. Considering that the overall Ru content of the film is 50%, the XPS data indicate that Ru enriches the near-surface region relative to the bulk and a depth-dependent Ru concentration profile that deviates from predictions based on Fick's law. It is important to note, however, that the cus- and subcus-sites probed by TPD represent only half of the cation sites in the first and second layers of the MO_2(110) structure; the remaining M_{br} and M_{subbr} (Figure 1) are not quantifiable by TPD of N_2 or O_t because those species bind to M_{cus} atoms and their binding strengths are largely unaffected by the identities of M_{br} and M_{subbr} cations. The gap in Ru contents between these TPD and XPS techniques suggests that M_{br} and M_{subbr} may be heavily occupied by Ir, which will be investigated by DFT techniques below. Nevertheless, the experimental results clearly demonstrate near-complete replacement of Ir by Ru in the cus and

https://doi.org/10.1021/acscatal.5c09252
ACS Catal. XXXX, XXX, XXX−XXX

subcus sites during prolonged thermal treatments, leading to substantial variations in adsorbate binding across the mixed Ir−Ru oxide surfaces.

Energetics of Near-Surface Cation Arrangements

DFT was used to calculate exchange energies associated with replacing an Ir atom with Ru in an $IrO_2(110)$ surface, referenced to their stoichiometric bulk rutile phases

$$(IrO_2)_n^{surf} + (RuO_2)_m^{bulk} \rightarrow (IrO_2)_{n-1}RuO_2^{surf} + (IrO_2)_m^{bulk}$$

and analogously for exchanging Ir into $RuO_2(110)$. These exchange energies quantify the relative stability of mixed metal oxide arrangements, with or without terminal O_t atoms, and therefore provide insight into the equilibrium surface configurations expected to form during high temperature (800 K) thermal treatments. The slow experimental evolution of the 22L-IrO_2/22L-RuO_2 surfaces (Figures 7 and 8) indicate that these structures are kinetically hindered and require >600 min of high-temperature treatment to approach their equilibrium cation distributions.

Exchanges were evaluated at both symmetrically distinct surface sites (M_{cus} and M_{br}) and subsurface positions up to 3 layers beneath the surface in a 6-layer $MO_2(110)$ slab. The bottom two layers were held fixed and not used as exchange sites. For exchanging Ir into RuO_2 surfaces ($Exch_{Ru\rightarrow Ir}$), we obtain endothermic exchange energies (20 and 10 kJ mol^{-1}) for the M_{cus} and M_{subcus} sites, respectively, whereas exchanges at all other sites are mildly exothermic (−1 to −10 kJ mol^{-1}; Figure 10). For exchanging Ru into IrO_2 surfaces ($Exch_{Ir\rightarrow Ru}$), the M_{cus} or M_{subcus} positions are strongly favorable (∼−27 kJ mol^{-1}), other subsurface exchanges are moderately favorable (∼−13 kJ mol^{-1}), and exchange into the M_{br} surface site is slightly exothermic (−1 kJ mol^{-1}). These trends in exchange energies were found to only slightly change with methodological choices such as the use of calculations without spin polarization, dispersive corrections using DFT-D3,[56,57] or comparing the RPBE and PBE exchange-correlation functionals, as shown in Table S5 of the SI, Section S15.

For both exchange types (Ru-into-IrO_2 and Ir-into-RuO_2), the exchange energies become negative 2−3 layers below the surface, consistent with the negative enthalpy of mixing reported for bulk $Ir_xRu_{1-x}O_2$ solid solutions.[24,58] For thick (6-layer) slabs, the exchange energies for these deeper layers are similar for both systems and show little dependence on whether sites lie beneath M_{cus} or M_{br} surface atoms, confirming that the surface and first subsurface layer (Figure 10a, layers 0 and 1) are most critical to predicting behavior. At low dopant levels, Ru preferences follow the trend: $M_{cus} \sim M_{subcus} > M_{subbr} > M_{br}$, while Ir preferences are generally the reverse: $M_{subbr} > M_{br} > M_{subcus} > M_{cus}$, with small deviations due to local coordination (which prevents the two exchange processes from being strict energetic inverses).

To span a broader composition range, we also computed exchange energies for 4-layer slab models in which the top two layers contained from 0% to 100% Ru (or Ir), while the bottom two layers were fixed as IrO_2 (or RuO_2). Focusing on Ru substitution into IrO_2-based surfaces, which is most relevant to our IrO_2/RuO_2 annealing experiments, we computed exchange energies into pure IrO_2 (Figure 10d) and into surfaces with 1−3 Ru atoms to assess the influence of neighboring Ru atoms. The presence of adjacent Ru atoms increased the exchange energies by only ≤ 2 kJ mol^{-1} (SI, Section S16), indicating a small energetic driving force for atomic dispersion of Ru in the IrO_2 surface layers. To explore the accessible configuration space, additional structures were generated by sequentially exchanging Ru into all cus sites (with maximally isolated Ru), followed by subcus, subbr, and then br sites, reflecting the site-preference order for dilute substitution into pure IrO_2 (Figure 10d). Because the exchange energies of cus and subcus sites are nearly identical, structures with mixed Ru occupancy of cus and subcus sites were also examined.

Across ∼100 RuO_2−IrO_2 model structures with 0−100% Ru in the top two layers, DFT predicts the following lowest-energy sequence. Ru first occupies cus sites, until half of them are filled (12.5% Ru), followed by a mixture of cus and subcus filling until all cus and half the subcus sites are occupied (37.5% Ru). Ru then continues to fill the remaining subcus sites until all cus and subcus positions are Ru (50% Ru). At this point, all binding sites are Ru/Ru_2, while the br and subbr sites remain as Ir. As the Ru content is increased further, Ru is predicted to substitute next into subbr positions and finally into br sites, yielding a fully Ru-substituted first and second layer (2L-RuO_2/2L-IrO_2 surface).

This focus on lowest-energy structures, however, neglects the role of configurational entropy and nonzero probability of occupying higher energy states at 800 K, particularly for Ru exchange into cus and subcus sites which have similar exchange energies. To account for this, we estimated the exchange energies of all (2^{16}) structures with Ru in cus and/or subcus sites. Exchange energies were estimated as

$$E_{Ex} = N_{cus}\varepsilon_{cus} + N_{subcus}\varepsilon_{subcus} + N_{c-c}\varepsilon_{c-c} + N_{c-sc}\varepsilon_{c-sc} + N_{sc-sc}\varepsilon_{sc-sc} \quad (1)$$

where N_j and ε_j represent the number and energy of Ru in each site (cus and subcus), and N_{j-j} and ε_{j-j} represent the number and energy of Ru in nearest-neighbor positions between cus sites (c−c), between cus and subcus sites (c−sc), and between subcus sites (sc−sc), see Table 1 and Section S16 of the SI for additional details on how these ε values were estimated. From these estimated exchange energies, Boltzmann weighting factors ($e^{E/RT}$) were computed for all surfaces, allowing calculation of weighted averages for structural features such as the Ru occupancy in cus and subcus sites and the resulting distribution among binding-site motifs.

Table 1. Parameters (kJ mol^{-1}) for Estimating Exchange Energies from Equation 1

	ε_{cus}	ε_{subcus}	ε_{c-c}	ε_{c-sc}	ε_{sc-sc}
Ru-in-IrO_2	−26.6	−25.6	1.2	0.2	1.7
Ru-in-IrO_2 with O_t	−37.6	−16.1	1.2	0.2	1.7

For stoichiometric surfaces, Figure 11a shows that Ru exhibits almost no inherent preference between cus and subcus sites, producing a nearly symmetric site distribution. Ir/Ir_2 sites are replaced first by Ir/RuIr and Ru/IrIr sites, followed by Ru/RuIr and Ir/Ru_2, and eventually by Ru/Ru_2 sites at high Ru contents (Figure 11b). Although Ru is slightly more stable in cus than subcus sites, Ir/RuIr outnumber Ru/IrIr sites because substituting Ru into a subcus site generates two Ir/RuIr sites, whereas substituting into a cus site generates only one Ru/IrIr site. The same symmetry-driven factor applies to Ru/RuIr vs Ir/Ru_2 motifs, favoring Ru/RuIr. These predicted site

https://doi.org/10.1021/acscatal.5c09252
ACS Catal. XXXX, XXX, XXX−XXX

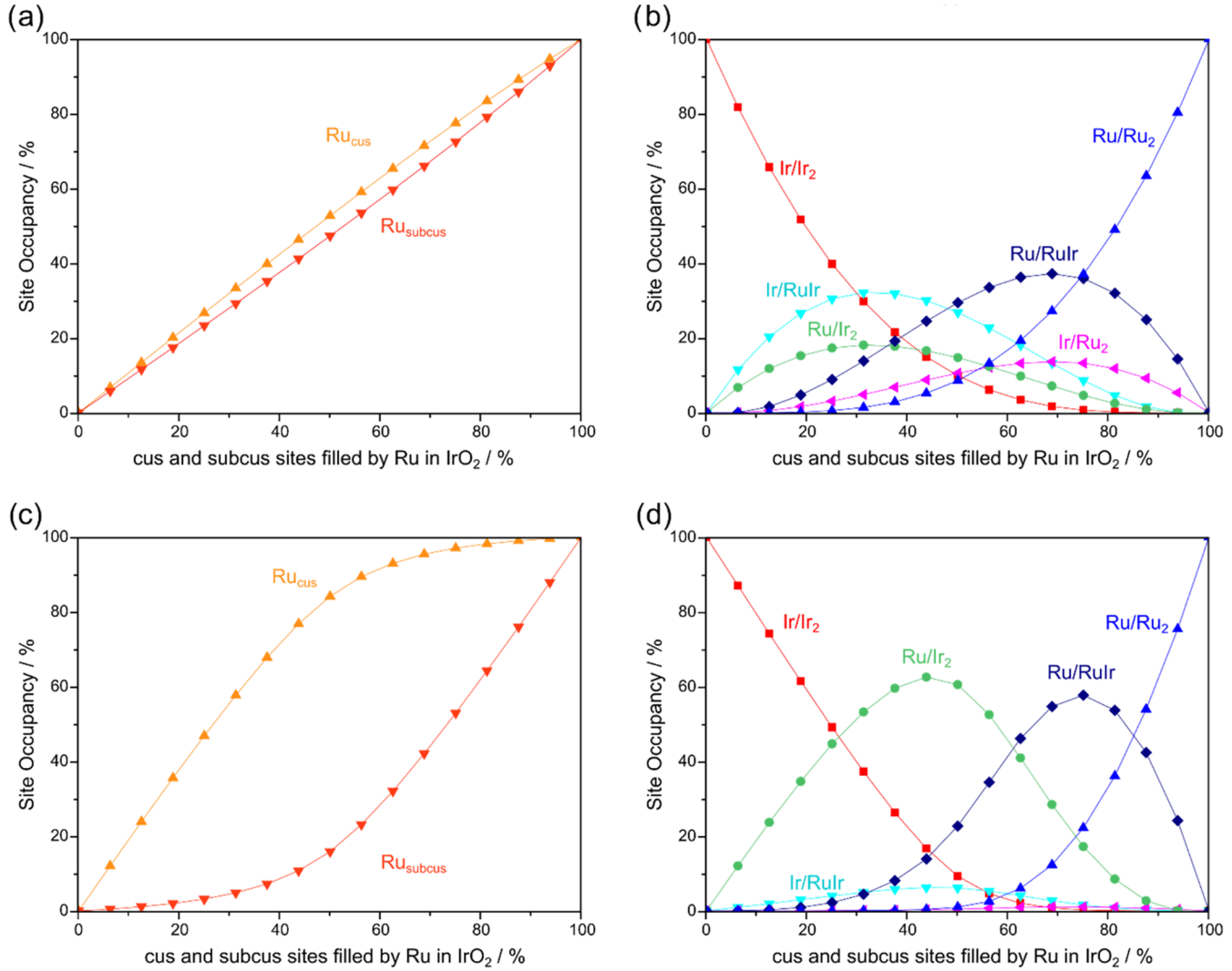

Figure 11. Percent of cus and subcus sites filled by Ru (a, c) and the binding site distributions (b, d) as Ru composition in cus and subcus goes from 0 to 100% in IrO_2-based surfaces. (a, b) Predictions for exchange on stoichiometric oxide surfaces. (c, d) Predictions for exchange on O_t-covered oxide surfaces.

distributions do not match the trends inferred from N_2 TPD (Figure 9), which show a clear bias toward Ru_{cus} enrichment (Figure 9a) and never exhibit significant populations of Ir/Ru_2 sites (Figure 9b).

As described above, Ru_{cus} binds O_t ~11 kJ mol^{-1} more strongly than Ir_{cus}, and Ir_{subcus} strengthens O_t binding by ~10 kJ mol^{-1} per Ir_{subcus} atom. Incorporating these shifts changes the predicted cus-subcus energy difference from ~1 kJ mol^{-1} (stoichiometric surface) to ~20 kJ mol^{-1} in favor of Ru_{cus}. With these O_t-modified parameters, a strong preference for Ru_{cus} emerges (Figure 11c), consistent with that inferred by N_2 TPD (Figure 9a). In the presence of O_t, Ir/Ir_2 sites are replaced sequentially by Ru/Ir_2, then Ru/RuIr, and finally Ru/Ru_2 at higher Ru contents (Figure 11d), again agreeing with the binding-site distributions derived from N_2 TPD (Figure 9b), although for simplicity our TPD analysis does not explicitly track Ru/RuIr sites.

A comparison of the computational and experimental results strongly suggests that oxygen adsorption governs the cus-subcus relative populations obtained during our heating treatments. In these treatments, the sample is continuously exposed to an O atom beam while being heated to 800 K, then cooled and held at 700 K for 10 min, with the O-exposure terminated only after cooling to 675 K. This protocol maintains fully oxidized structures (Figure 5), but avoids significant O_t accumulation because oxygen dosing ceases above the temperature(s) for associative O_t desorption in UHV (Figures 2 and 8). At 800 K, cation intermixing is relatively facile within the oxide structures. However, because the O_t coverage remains low (<0.5%) at the combined O and O_2 flux used here (~0.15 ML s^{-1}), the near-surface cation distributions at 800 K are expected to reflect stoichiometrically terminated oxides. Under these conditions, the strong Ru−Ir exchange driving force (Figure 10) should enrich both cus and subcus sites in Ru, yielding comparable occupancies of each. By contrast, although adsorbate coverages are high during TPD, the N_2 and O_2 TPD spectra remain unchanged after repeated measurements (SI, Section S4), indicating that thermal energies below ~650 K are insufficient to overcome barriers required for adsorbate-stimulated cation restructuring.

The strong experimental preference for Ru in cus sites may develop during cooling below 800 K. As the sample cools under the combined O and O_2 flux, the equilibrium O_t coverage increases substantially. For example, we estimate

https://doi.org/10.1021/acscatal.5c09252
ACS Catal. XXXX, XXX, XXX−XXX

that the steady-state O_t coverage at 725 K is ~2.5%—approximately five times greater than at 800 K—and that the surface is exposed to a cumulative O atom fluence of ~0.20 ML during cooling to 725 K. Although these O_t coverages and exposures are low, they may be sufficient to promote Ru−Ir interchange between cus and subcus sites, potentially driving the enhanced Ru_{cus} and Ru/Ir_2 populations toward those predicted for O_t-terminated surfaces. Notably, our prior work shows that the cus/subcus cation arrangements of epitaxial IrO_2/RuO_2 films remain stable during repeated O atom exposures at 700 K, suggesting that any O_t-stimulated restructuring requires higher temperatures.[23] Consistent with this observation, the negligible changes in cation populations during subsequent TPD indicate that the Ru_{cus} enrichment observed here is kinetically stabilized below ~700 K, even at negligible O_t coverage. As a result, the cation distributions do not revert to the more even partitioning of Ru between cus and subcus sites expected for stoichiometrically terminated surfaces.

An alternative possibility is that the cation exchange preferences at 800 K differ from the DFT predictions because the oxide structure becomes partially disordered and oxygen mobility is high. At 800 K, the oxide begins to decompose in the absence of an O-beam, implying a dynamically evolving structure in which oxygen diffusion (e.g., between O_{br} and O_t sites), desorption, and readsorption occur rapidly. Motivated by this behavior, we calculated exchange energies into surfaces in which a O_{br} atom has diffused into a cus site (forming an O_t adsorbate and leaving a bridging oxygen vacancy), and find that those exchange energies are very similar to those observed in the presence of O_t atoms (Table S7, SI, Section S17). Similarly, we calculated the effects of surface oxygen vacancies (at both O_{br} and O_{3f} sites) and find that those vacancies do not significantly affect Ru-into-IrO_2 exchange energies for the cus or subcus sites (Table S7, SI, Section S17). Thus, under the 800 K treatment conditions, oxygen transport to and on the surface may mediate Ru enrichment in cus sites in a manner that effectively mimics the influence of high O_t coverages, even at conditions that disfavor oxygen adsorption.

Cation Intermixing of a $RuO_2/IrO_2/RuO_2$ Layered Structure

Our results with both the 6L-IrO_2/22L-RuO_2 and 22L-IrO_2/22L-RuO_2 layered structures show that Ru replaces Ir in cus- and subcus-sites but that small quantities of Ir remain in subcus-sites after prolonged heating. DFT calculations further suggest that enhanced O_t binding provides an energetic driving force for retaining Ir in subcus sites. These observations motivated us to investigate cation intermixing in an initial ~5L-RuO_2/6L-IrO_2/22L-RuO_2 layered structure, with the goal of determining whether the heating protocol would similarly drive Ir into subcus positions to stabilize O_t binding, when Ir is initially positioned several layers below the surface.

Heating the 5L-RuO_2/6L-IrO_2/22L-RuO_2 structure produces negligible Ir occupation in the cus- and subcus-sites. The molecular N_2 and associative O_t TPD shapes remain unchanged after up to 200 min of heating (Section S18, Figure S17), indicating that Ir does not replace Ru in either site. In contrast, Ru nearly completely replaces Ir at cus- and subcus-sites (~100% and 91%) when an initial 6L-IrO_2/22L-RuO_2 structure is heated under identical conditions (SI, Section S14, Figure S15a). XPS further shows that the near-surface Ir concentration steadily decreases as the 5L-RuO_2/6L-IrO_2/22L-RuO_2 structure is heated (Figures S18 and S19), dropping from ~30% to ~16% with no indication of leveling off after 200 min. This demonstrates that intermixing with the RuO_2 drives Ir out of the XPS sampling depth. Notably, simple dilution of Ir into the underlying 22-layer RuO_2 film would decrease the XPS-derived Ir fraction from 30% to ~10% if the top five layers remained pure RuO_2. The observed ~16% value is only reproduced if some Ir also occupies near-surface layers. Together, the XPS and TPD data indicate that Ir negligibly occupies cus and subcus sites after heating, but likely incorporates into a fraction of br and subbr sites while also dispersing deeper into the bulk.

A plausible explanation for the absence of Ir_{subcus} formation in the 5L-RuO_2/6L-IrO_2/22L-RuO_2 structure is that cation intermixing at 800 K is governed primarily by the thermodynamic site-preferences of stoichiometric surfaces, whereas kinetic limitations subsequently restrict cation rearrangements as the O_t coverage increases at lower temperature. For stoichiometric surfaces, DFT predicts that Ru strongly favors cus- and subcus-sites, whereas Ir exhibits a modest preference for br and subbr sites and is more stable in bulk-sites of RuO_2 (Figure 10). As the sample cools below 800 K, the O_t coverage increases; however, the Ir_{subcus} population remains negligible even though formation of Ru/Ir_2 and Ru/RuIr motifs would strengthen O_t binding.

This behavior suggests that Ir initially located in br, subbr or deeper lying sites either cannot overcome kinetic barriers to migrate into subcus sites at these lower temperatures, or that exchange from these sites into subcus sites remains thermodynamically unfavorable even on O_t-terminated surfaces. In contrast, Ir−Ru interchange between cus and subcus sites is thermodynamically favorable for O_t-terminated surfaces and appears kinetically accessible above ~700 K, consistent with the strong preference for Ru/Ir_2 motifs observed after annealing IrO_2/RuO_2 structures. Ir_{subcus} formation may likewise be disfavored in the dynamically evolving oxide structures present during annealing at 800 K, even if oxygen adsorption promotes Ru enrichment at cus sites under those conditions and effectively mimics the influence of O_t atoms.

DISCUSSION

The present study demonstrates that heating layered IrO_2/RuO_2 structures under mildly oxidizing conditions provides an effective route for synthesizing atomically mixed $Ir_xRu_{1-x}O_2(110)$ surfaces with tunable M_{cus}/M_{subcus} arrangements. Because adsorbate binding is highly sensitive to these local cation arrangements, and because the structures remain stable during TPD up to at least 650 K—conditions relevant to heterogeneous catalysis[13−17,59−61]—our findings open new opportunities to systematically investigate how local cation identity and concentration control the chemical properties of $Ir_xRu_{1-x}O_2(110)$, including surfaces enriched in atomically dispersed Ru or Ir sites.

Our synthetic approach may also prove valuable for tuning surface cation distributions in nanoparticles, enabling the preparation of high surface-area catalysts with compositionally tailored reactivity for practical applications. Moreover, the present results show that the localized influence of M_{cus} and M_{subcus} cations, previously identified for epitaxial heterostructures,[23] extends to atomically mixed $Ir_xRu_{1-x}O_2$ surfaces. This finding is significant because it demonstrates that local cation arrangements can strongly modify adsorbate binding—and thus reaction barriers—providing a mechanistic framework for interpreting composition-dependent trends in $Ir_xRu_{1-x}O_2$

https://doi.org/10.1021/acscatal.5c09252
ACS Catal. XXXX, XXX, XXX−XXX

catalysis. In addition, our results suggest that probe-molecule TPD might be able to quantify near-surface cation arrangements in more complex nanocatalysts, information essential for establishing synthesis−structure−function relationships in $Ir_xRu_{1-x}O_2$ and, potentially, in other mixed-metal oxide catalysts. Establishing connections between our thin-film results and nanoparticles will require future work to explore the influence of defects and multiple facets on TPD profiles; nevertheless, such connections are promising given the dominance of the (110) facet on $Ir_xRu_{1-x}O_2$ nanocrystals[39,62] as well as the large differences in adsorbate binding among M_{cus}/M_{subcus} motifs. Indeed, recent work highlights the importance of controlling near-surface cation distributions for enhancing the stability of $Ir_xRu_{1-x}O_2$ OER catalysts while minimizing Ir usage.[24] Our study complements these efforts by providing a sensitive experimental method (probe-molecule TPD) to directly characterize site distributions, a capability that prior studies have lacked.

An important future effort is to assess the stability of variable composition $Ir_xRu_{1-x}O_2$ surfaces under catalytic conditions. The present results provide evidence that oxygen adsorption readily alters the cus−subcus distributions at low oxygen pressure (~5×10^{-7} Torr) above ~700 K, whereas restructuring is negligible up to 650 K during N_2 and O_2 TPD. Establishing conditions under which predefined surface-site motifs remain stable or, conversely, when adsorbate-induced restructuring becomes significant, will be essential for relating catalyst performance to surface composition.

Future efforts should also aim to characterize the cations occupying br and subbr sites and to determine how these sites influence surface chemical properties. Although M_{br} and M_{subbr} atoms have minimal impact on adsorbate binding at M_{cus} sites, and thus cannot be effectively probed using N_2 or O_t TPD, they may still modify the binding strength and reactivity of O_{br} species. Systematic studies of $Ir_xRu_{1-x}O_2$ surface reactions with reductants such as H_2 and CO may therefore reveal how M_{br} and M_{subbr} identity modulate O_{br} reactivity and provide additional strategies for tuning surface chemistry.

Finally, although the present experiments could, in principle, provide insights into cation diffusivity in mixed $Ir_xRu_{1-x}O_2$, we refrain from extracting quantitative diffusivities due to uncertainties in the oxide structures at elevated temperature. The initial films likely contain grain boundaries and other defects,[18] and their structures evolve dynamically during thermal treatments, generating transient defects such as oxygen vacancies. Because such defects likely play an important role in mediating cation interdiffusion, meaningful modeling will require additional structural information and ideally operando characterization.

SUMMARY

The present study synthesized $Ir_xRu_{1-x}O_2(110)$ surfaces with variable cation arrangements by heating layered IrO_2/RuO_2 heterostructures under mild oxidizing conditions in UHV. We show that the local M_{cus}/M_{subcus} arrangements on these surfaces can be quantitatively assessed using N_2 and O_t TPD measurements due to the strong and localized influence of these cations on adsorbate binding. Our results demonstrate that Ru preferentially diffuses toward the surface when IrO_2/RuO_2 layered structures are annealed in oxygen, increasing the Ru concentration within the XPS sampling depth above the bulk-average value. Quantitative analysis of N_2 TPD data further reveals that Ru substitutes for Ir first in cus-sites and only begins to populate subcus-sites once the Ru_{cus} population approaches saturation (~100%). After prolonged heating, the surface is dominated by Ru/Ru_2 sites characteristic of pure $RuO_2(110)$, with only minor populations of Ru/Ir_2 or Ru/RuIr motifs.

DFT calculations are consistent with these experimental results. They predict a strong but nearly equal energetic driving force for Ru to occupy cus and subcus sites of stoichiometrically terminated $Ir_xRu_{1-x}O_2(110)$, and reveal moderate preferences for Ir to reside in br and subbr sites. Importantly, DFT also shows that adsorbed O_t atoms strongly favor Ru incorporation into cus-sites over subcus-sites, and the predicted binding site distributions for O_t-rich surfaces closely match those inferred from N_2 TPD. These findings indicate that oxygen adsorption plays a central role in determining the relative cus-subcus populations established during our heating protocol of IrO_2/RuO_2 layered structures. The enhanced O_t binding on Ru_{cus} relative to Ir_{cus}, together with the additional stabilization provided by Ir_{subcus} atoms, promotes Ru−Ir interchange between cus and subcus sites and drives the surface toward Ru-enriched cus arrangements. Overall, this work provides new insight into both the synthesis and characterization of $Ir_xRu_{1-x}O_2(110)$ surfaces with tunable cation arrangements and compositions. The results illustrate a general strategy for producing mixed-oxide surfaces with controllable local environments and suggest that TPD using structure-sensitive probe molecules might serve as a powerful tool for elucidating cation distributions on more complex nanocatalysts. These advances can help enable rational design of mixed Ir−Ru oxide catalysts with tailored chemical properties.

ASSOCIATED CONTENT

Supporting Information

The Supporting Information is available free of charge at https://pubs.acs.org/doi/10.1021/acscatal.5c09252.

Estimation of thickness of base-$RuO_2(110)$; estimation of IrO_2 and RuO_2 thickness; experimental details; repeated TPD measurements from 6-layer and 22-layer IrO_2 on RuO_2; estimation of molecular N_2 and associative O_t TPD temperatures; DFT calculated O_2 adsorption and dissociation pathways on different mixed oxide configurations; Paired O_t binding energies on mixed $IrO_2-RuO_2(110)$ surfaces; O 1s peak from mixing of a 22-L IrO_2 and 22-L RuO_2 film; XPS and TPD spectra from heating of a 6-layer IrO_2 film on 22-layer RuO_2; LEED images from 22-layer film after mixing experiments; calculation of relative sensitivity factor and XPS-derived atomic percentages; details of TPD spectral fitting; fits from heating of a 6-layer IrO_2 film on 22-layer RuO_2; quantitative analysis from 6-layer IrO_2 on 22-layer RuO_2; exchange energy computations using different functionals; influence of neighboring atoms on exchange energies of Ir and Ru; exchange energy computations in the presence of oxygen vacancies; TPD and XPS spectra from mixing experiments on 5L-RuO_2 film grown on 6-L IrO_2 film (PDF)

AUTHOR INFORMATION

Corresponding Authors

David Hibbits − *Department of Chemical Engineering, University of Florida, Gainesville, Florida 32611, United*

https://doi.org/10.1021/acscatal.5c09252
ACS Catal. XXXX, XXX, XXX−XXX

States; Davidson School of Chemical Engineering, Purdue University, West Lafayette, Indiana 47907, United States; orcid.org/0000-0001-8606-7000; Email: hibbitts@purdue.edu

Jason F. Weaver − *Department of Chemical Engineering, University of Florida, Gainesville, Florida 32611, United States;* orcid.org/0000-0002-6777-4727; Email: weaver@che.ufl.edu

Authors

Suriya Ramasubramanian − *Department of Chemical Engineering, University of Florida, Gainesville, Florida 32611, United States*

Jisu Shin − *Department of Chemical Engineering, University of Florida, Gainesville, Florida 32611, United States; Davidson School of Chemical Engineering, Purdue University, West Lafayette, Indiana 47907, United States*

Tanmayee Kulkarni − *Department of Chemical Engineering, University of Florida, Gainesville, Florida 32611, United States*

Abbul Hasan − *Department of Chemical Engineering, University of Florida, Gainesville, Florida 32611, United States*

Complete contact information is available at: https://pubs.acs.org/10.1021/acscatal.5c09252

Author Contributions

§S.R. and J.S. contributed equally to this work.

Notes

The authors declare no competing financial interest.

■ ACKNOWLEDGMENTS

We gratefully acknowledge the National Science Foundation for financial support (NSF CHEM #2102211) and computational resources (via ACCESS). Computational resources were also provided by University of Florida Research Computing.

■ REFERENCES

(1) Chaudhary, P.; Zagalskaya, A.; Over, H.; Alexandrov, V. Strain-Dependent Activity-Stability Relations in RuO_2 and IrO_2 Oxygen Evolution Catalysts. *ChemElectroChem* **2024**, *11*, No. e202300659.

(2) Song, J. J.; Wei, C.; Huang, Z. F.; Liu, C. T.; Zeng, L.; Wang, X.; Xu, Z. C. J. A review on fundamentals for designing oxygen evolution electrocatalysts. *Chem. Soc. Rev.* **2020**, *49*, 2196−2214.

(3) Chen, F. Y.; Wu, Z. Y.; Adler, Z.; Wang, H. T. Stability challenges of electrocatalytic oxygen evolution reaction: From mechanistic understanding to reactor design. *Joule* **2021**, *5*, 1704−1731.

(4) Ma, Z.; Zhang, Y.; Liu, S. Z.; Xu, W. Q.; Wu, L. J.; Hsieh, Y. C.; Liu, P.; Zhu, Y. M.; Sasaki, K.; Renner, J. N.; Ayers, K. E.; Adzic, R. R.; Wang, J. X. Reaction mechanism for oxygen evolution on RuO_2, IrO_2, and RuO_2@IrO_2 core-shell nanocatalysts. *J. Electroanal. Chem.* **2018**, *819*, 296−305.

(5) Kasian, O.; Geiger, S.; Stock, P.; Polymeros, G.; Breitbach, B.; Savan, A.; Ludwig, A.; Cherevko, S.; Mayrhofer, K. J. J. On the Origin of the Improved Ruthenium Stability in RuO_2-IrO_2 Mixed Oxides. *J. Electrochem. Soc.* **2016**, *163*, F3099−F3104.

(6) Gu, X. K.; Camayang, J. C. A.; Samira, S.; Nikolla, E. Oxygen evolution electrocatalysis using mixed metal oxides under acidic conditions: Challenges and opportunities. *J. Catal.* **2020**, *388*, 130−140.

(7) Dickens, C. F.; Kirk, C.; Norskov, J. K. Insights into the Electrochemical Oxygen Evolution Reaction with ab Initio Calculations and Microkinetic Modeling: Beyond the Limiting Potential Volcano. *J. Phys. Chem. C* **2019**, *123*, 18960−18977.

(8) Li, J.; Tian, W. C.; Li, Q.; Zhao, S. L. Acidic Oxygen Evolution Reaction: Fundamental Understanding and Electrocatalysts Design. *ChemSusChem* **2024**, *17*, No. e202400239.

(9) Ying, J.; Chen, J. B.; Xiao, Y. X.; de Torresi, S. I. C.; Ozoemena, K. I.; Yang, X. Y. Recent advances in Ru-based electrocatalysts for oxygen evolution reaction. *J. Mater. Chem. A* **2023**, *11*, 1634−1650.

(10) Vazhayil, A.; Vazhayal, L.; Thomas, J.; Ashok, C. S.; Thomas, N. A comprehensive review on the recent developments in transition metal-based electrocatalysts for oxygen evolution reaction. *Appl. Surf. Sci. Adv.* **2021**, *6*, No. 100184.

(11) Owe, L. E.; Tsypkin, M.; Wallwork, K. S.; Haverkamp, R. G.; Sunde, S. Iridium-ruthenium single phase mixed oxides for oxygen evolution: Composition dependence of electrocatalytic activity. *Electrochim. Acta* **2012**, *70*, 158−164.

(12) Li, G. Q.; Li, S. T.; Ge, J. J.; Liu, C. P.; Xing, W. Discontinuously covered IrO_2-RuO_2@Ru electrocatalysts for the oxygen evolution reaction: how high activity and long-term durability can be simultaneously realized in the synergistic and hybrid nanostructure. *J. Mater. Chem. A* **2017**, *5*, 17221−17229.

(13) Hsiao, L. Y.; Hagelin-Weaver, H. Structure Sensitivity of TiO_2-Supported IrO_2 Catalysts in the Complete Oxidation of Methane. *ACS Catal.* **2025**, *15*, 17255−17270.

(14) Khalid, O.; Luciano, A. S.; Drazic, G.; Over, H. Mixed $Ru_xIr_{1-x}O_2$ supported on rutile TiO_2: Catalytic methane combustion, a model study. *ChemCatChem* **2021**, *13*, 3983−3994.

(15) Pope, C.; Yun, J. W.; Reddy, R.; Jamir, J.; Asthagiri, A.; Weaver, J. F. Surface intermediates identified using IR spectroscopy during the catalytic oxidation of C_2H_6 on IrO_2(110) at near-ambient pressures. *J. Catal.* **2026**, *453*, No. 116514.

(16) Jamir, J.; Pope, C.; Ramasubramanian, S.; Mehar, V.; Shi, J. J.; Weaver, J. F. Influence of Water on the Catalytic Oxidation of Ethane on IrO_2(110). *ACS Catal.* **2024**, *14*, 7062−7073.

(17) Jamir, J.; Kim, M.; Pope, C.; Asthagiri, A.; Weaver, J. F. Linking operando spectroscopy with microkinetic modeling to unravel the catalytic mechanism for CH_4 oxidation on IrO_2(110). *ACS Catal.* **2023**, *13*, 14598−14613.

(18) Abb, M. J. S.; Herd, B.; Over, H. Template-assisted growth of ultrathin single-crystalline IrO_2(110) films on RuO_2(110)/Ru(0001) and its thermal stability. *J. Phys. Chem. C* **2018**, *122*, 14725−14732.

(19) Martin, R.; Kim, M.; Lee, C. J.; Shariff, M. S.; Feng, F.; Meyer, R. J.; Asthagiri, A.; Weaver, J. F. Molecular chemisorption of N_2 on IrO_2(110). *J. Chem. Phys.* **2020**, *152*, No. 074712.

(20) Mcdaniel, C. L.; Schneider, S. J. Phase Relations in Ru-Ir-O_2 System in Air. *J. Res. Natl. Bur. Stand., Sect. B* **1969**, *73*, No. 213.

(21) Escudero-Escribano, M.; Pedersen, A. F.; Paoli, E. A.; Frydendal, R.; Friebel, D.; Malacrida, P.; Rossmeisl, J.; Stephens, I. E. L.; Chorkendorff, I. Importance of Surface IrO_x in Stabilizing RuO_2 for Oxygen Evolution. *J. Phys. Chem. B* **2018**, *122*, 947−955.

(22) Man, I. C. *Theoretical Study of Electro-Catalysts for Oxygen Evolution*; Technical University of Denmark: 2011.

(23) Ramasubramanian, S.; Shin, J.; Lee, C. J.; Sudarshan, C.; Almarshad, O.; Orduz, A. L.; Meyer, R. J.; Plaisance, C.; Hibbitts, D.; Weaver, J. F. Modified Adsorption Energies on Single-Layer IrO_2 and RuO_2 Films of IrO_2-RuO_2 Heterostructures: Localized Effect of Subsurface Metal-Oxygen Ligands. *ACS Catal.* **2025**, *15*, 11134−11149.

(24) Qiu, C.; Sellers, C.; Wu, Z. Y.; Cullen, D. A.; Stavitski, E.; Tayal, A.; Wi, T. U.; Kodali, M.; Erb, B.; Smeltz, A.; Chen, F. Y.; Feng, Y. G.; Yu, Z.; Elgazzar, A.; Terlier, T.; Senftle, T. P.; Wang, H. T. Low-iridium stabilized ruthenium oxide anode catalyst for durable proton-exchange membrane water electrolysis. *Nat. Nanotechnol.* **2025**, *20*, 1787−1795.

(25) Kresse, G.; Hafner, J. Abinitio Molecular-Dynamics for Liquid-Metals. *Phys. Rev. B* **1993**, *47*, No. 558.

(26) Kresse, G.; Hafner, J. Ab-initio molecular-dynamics simulation of the liquid-metal amorphous-semiconductor transition in germanium. *Phys. Rev. B* **1994**, *49*, No. 14251.

(27) Kresse, G.; Furthmuller, J. Efficient iterative schemes for ab initio total-energy calculations using a plane-wave basis set. *Phys. Rev. B* **1996**, *54*, No. 11169.
(28) Kresse, G.; Furthmuller, J. Efficiency of ab-initio total energy calculations for metals and semiconductors using a plane-wave basis set. *Comput. Mater. Sci.* **1996**, *6*, 15−50.
(29) Kravchenko, P.; Plaisance, C.; Hibbitts, D.A new computational interface for catalysis *ChemRxiv* 2019 DOI: 10.26434/chemrxiv.8040737.
(30) Perdew, J. P.; Burke, K.; Ernzerhof, M. Generalized gradient approximation made simple. *Phys. Rev. Lett.* **1996**, *77*, No. 3865.
(31) Blöchl, P. E. Projector augmented-wave method. *Phys. Rev. B* **1994**, *50*, No. 17953.
(32) Kresse, G.; Joubert, D. From ultrasoft pseudopotentials to the projector augmented-wave method. *Phys. Rev. B* **1999**, *59*, No. 1758.
(33) Ping, Y.; Galli, G.; Goddard, W. A. Electronic Structure of IrO_2: The Role of the Metal d Orbitals. *J. Phys. Chem. C* **2015**, *119*, 11570−11577.
(34) Wang, C. C.; Siao, S. S.; Jiang, J. C. Density Functional Theory Study of NH_x (x = 0−3) and N_2 Adsorption on IrO_2(110) Surfaces. *J. Phys. Chem. C* **2010**, *114*, 18588−18593.
(35) Kim, Y. D.; Seitsonen, A. P.; Over, H. Adsorption characteristics of CO and N-2 on RuO2(110). *Phys. Rev. B* **2001**, *63*, No. 115419.
(36) Li, T.; Kim, M.; Liang, Z.; Asthagiri, A.; Weaver, J. Hydrogen oxidation on oxygen-rich IrO_2(110). *Catal., Struct. React.* **2018**, *4*, 1−13.
(37) Kim, M.; Franklin, A.; Martin, R.; Feng, F.; Li, T.; Liang, Z.; Asthagiri, A.; Weaver, J. Adsorption and oxidation of CH_4 on oxygen-rich IrO_2(110). *J. Phys. Chem. C* **2019**, *123*, 27603−27614.
(38) Kim, Y. D.; Seitsonen, A. P.; Wendt, S.; Wang, J.; Fan, C.; Jacobi, K.; Over, H.; Ertl, G. Characterization of various oxygen species on an oxide surface: RuO_2(110). *J. Phys. Chem. B* **2001**, *105*, 3752−3758.
(39) Over, H. Surface chemistry of ruthenium dioxide in heterogeneous catalysis and electrocatalysis: From fundamental to applied research. *Chem. Rev.* **2012**, *112*, 3356−3426.
(40) Weaver, J. F. Surface chemistry of late transition metal oxides. *Chem. Rev.* **2013**, *113*, 4164−4215.
(41) Gerrard, A. L.; Chen, J. J.; Weaver, J. F. Oxidation of nitrided Si(100) by gaseous atomic and molecular oxygen. *J. Phys. Chem. B* **2005**, *109*, 8017−8028.
(42) Rai, R.; Li, T.; Liang, Z.; Kim, M.; Asthagiri, A.; Weaver, J. F. Growth and termination of an IrO_2(100) film on Ir(111). *Surf. Sci.* **2016**, *652*, 213−221.
(43) Kan, H. H.; Shumbera, R. B.; Weaver, J. F. Adsorption and abstraction of oxygen atoms on Pd(111): Characterization of the precursor to PdO formation. *Surf. Sci.* **2008**, *602*, 1337−1346.
(44) Cartas, W.; Rai, R.; Sathe, A.; Schaefer, A.; Weaver, J. F. Oxidation of a Tb_2O_3(111) thin film on Pt(111) by gas-phase oxygen atoms. *J. Phys. Chem. C* **2014**, *118*, 20916−20926.
(45) Abb, M. J. S.; Weber, T.; Langsdorf, D.; Koller, V.; Gericke, S. M.; Pfaff, S.; Busch, M.; Zetterberg, J.; Preobrajenski, A.; Gronbeck, H.; Lundgren, E.; Over, H. Thermal stability of single-crystalline IrO_2(110) layers: Spectroscopic and adsorption studies. *J. Phys. Chem. C* **2020**, *124*, 15324−15336.
(46) Pope, C.; Yun, J.; Reddy, R.; Jamir, J.; Kim, D.; Kim, M.; Asthagiri, A.; Weaver, J. F. Surface chlorination of IrO_2(110) by HCl. *J. Chem. Phys.* **2024**, *161*, No. 064704.
(47) Lee, C. J.; Vashishtha, S.; Shariff, M.; Zou, F. R.; Shi, J. J.; Meyer, R. J.; Weaver, J. F. Kinetics and selectivity of methane oxidation on an IrO_2(110) film. *J. Phys.: Condens. Matter* **2022**, *34*, No. 284002.
(48) Li, T.; Rai, R.; Liang, Z.; Kim, M.; Asthagiri, A.; Weaver, J. F. Adsorption and oxidation of n-butane on the stoichiometric RuO_2(110) surface. *J. Phys. Chem. C* **2016**, *120*, 9863−9873.
(49) Li, T.; Kim, M.; Liang, Z.; Asthagiri, A.; Weaver, J. F. Dissociative chemisorption and oxidation of H_2 on the stoichiometric IrO_2(110) surface. *Top. Catal.* **2018**, *61*, 397−411.
(50) Liang, Z.; Li, T.; Kim, M.; Asthagiri, A.; Weaver, J. F. Low-temperature activation of methane on the IrO_2(110) surface. *Science* **2017**, *356*, 299−303.
(51) Powell, C. J.; Jablonski, A.; National Institute of Standards and Technology. Electron Inelastic-Mean-Free-Path Database 2025 https://www.nist.gov/srd/nist71. (accessed December 25, 2025).
(52) Martin, R.; Kim, M.; Lee, C. J.; Mehar, V.; Albertin, S.; Hejral, U.; Merte, L. R.; Lundgren, E.; Asthagiri, A.; Weaver, J. F. High resolution x-ray photoelectron spectroscopy of an IrO_2(110) film on Ir(100). *J. Phys. Chem. Lett.* **2020**, *11*, 7184−7189.
(53) Novotny, Z.; Tobler, B.; Artiglia, L.; Fischer, M.; Schreck, M.; Raabe, J.; Osterwalder, J. Kinetics of the thermal oxidation of Ir(100) toward IrO_2 studied by ambient-pressure x-ray photoelectron spectroscopy. *J. Phys. Chem. Lett.* **2020**, *11*, 3601−3607.
(54) Over, H.; Seitsonen, A. P.; Lundgren, E.; Wiklund, M.; Andersen, J. N. Spectroscopic characterization of catalytically active surface sites of a metallic oxide. *Chem. Phys. Lett.* **2001**, *342*, 467−472.
(55) Over, H.; Seitsonen, A. P.; Lundgren, E.; Smedh, M.; Andersen, J. N. On the origin of the Ru-3d(5/2) satellite feature from RuO2(110). *Surf. Sci.* **2002**, *504*, L196−L200.
(56) Grimme, S.; Antony, J.; Ehrlich, S.; Krieg, H. A consistent and accurate ab initio parametrization of density functional dispersion correction (DFT-D) for the 94 elements H-Pu. *J. Chem. Phys.* **2010**, *132*, No. 154104.
(57) Grimme, S.; Ehrlich, S.; Goerigk, L. Effect of the Damping Function in Dispersion Corrected Density Functional Theory. *J. Comput. Chem.* **2011**, *32*, 1456−1465.
(58) Tao, Z. H.; Lv, N.; Zhao, H. Y.; Luo, X.; Li, Z. L.; Yu, J.; Chen, L.; Liu, X. P.; Mu, S. C. Dual active site-mediated Ir single-atom-doped RuO_2 catalysts for highly efficient and stable water splitting. *Chem. Sci.* **2024**, *15*, 16796−16803.
(59) Martin, R.; Lee, C. J.; Mehar, V.; Kim, M.; Asthagiri, A.; Weaver, J. F. Catalytic Oxidation of Methane on IrO_2(110) Films Investigated Using Ambient-Pressure X-ray Photoelectron Spectroscopy. *ACS Catal.* **2022**, *12*, 2840−2853.
(60) Martin, R.; Jamir, J.; Kim, M.; Lee, C. J.; Mehar, V.; Asthagiri, A.; Weaver, J. F. Activity of Ir(100) and IrO_2(110) for the Catalytic Oxidation of Methane. *J. Phys. Chem. C* **2022**, *126*, 15156−15166.
(61) Khalid, O.; Weber, T.; Drazic, G.; Djerdj, I.; Over, H. Mixed RuxIr1-xO2 Oxide Catalyst with Well-Defined and Varying Composition Applied to CO Oxidation. *J. Phys. Chem. C* **2020**, *124*, 18670−18683.
(62) Sen, F. G.; Kinaci, A.; Narayanan, B.; Gray, S. K.; Davis, M. J.; Sankaranarayanan, S. K. R. S.; Chan, M. K. Y. Towards accurate prediction of catalytic activity in IrO_2 nanoclusters via first principles-based variable charge force field. *J. Mater. Chem. A* **2015**, *3*, 18970−18982.

https://doi.org/10.1021/acscatal.5c09252
ACS Catal. XXXX, XXX, XXX−XXX